Vigyan Vardhan
Blessed Foundation

e-ISSN: 3048-460X

Peer-reviewed, Multidisciplinary Journal

CNS&E

Current Natural Sciences & Engineering

Future Generation & Storage of Green Energy: A Rescue for Earth's Sustainability!

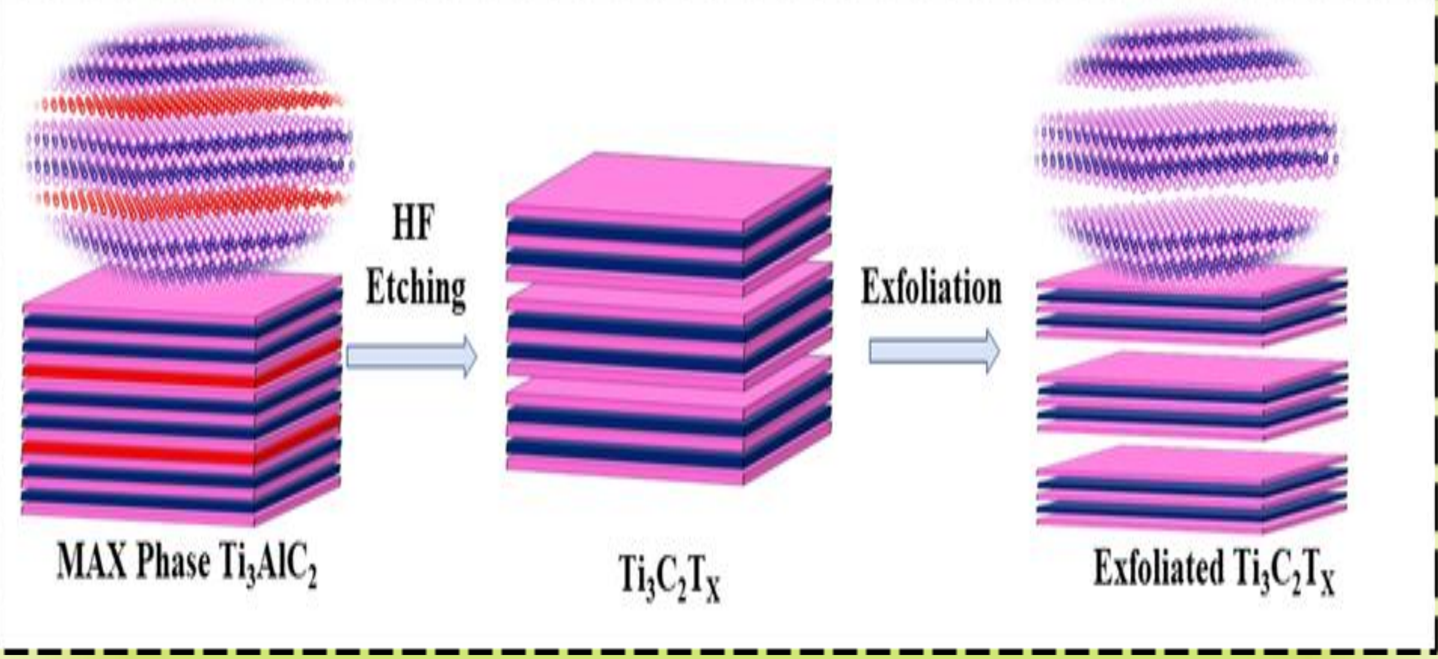

http://doi.org/10.63015/cnse-2026.3.1

Volume 3 Issue 1, June 2026

About CNS&E

Current Natural Sciences & Engineering (CNS&E) Journal publishes new, innovative and cutting-edge research in Natural sciences including physical, chemical, biological, agricultural and environmental sciences, metrology, and other related interdisciplinary fields. Scientific research results in the form of high-quality manuscripts, review articles, mini-reviews, reports, news and short communications are highly welcome.

CNS&E is a hybrid, bimonthly, multidisciplinary journal published by the Vigyanvardhan Blessed Foundation (VBF), a non-profit organization working to disseminate science for the betterment of society.

Scope: CNS&E journal has a broad multidimensional scope. It publishes research in the areas of:

- ☐ Hydrogen & Renewable Energy
- ☐ Environmental Sciences & Hydroelectric Cell
- ☐ Artificial Intelligence Convergence in S&T
- ☐ Net Carbon Zero &Earth Sustainability
- ☐ Condensed Matter & Nanomaterials
- ☐ Health Science & Technology
- ☐ Nuclear Science: Health & Society
- ☐ Measurement Science & Industrial Research
- ☐ Digital & Sustainable Agriculture
- ☐ Smart Engineering Materials & Sensors

Publication Policy: The journal maintains integrity and high ethical values. Submitted manuscripts are peer-reviewed and evaluated for novel scientific content irrespective of its origin. The information about a submitted manuscript will be confidential and will not be disclosed other than Chief Editor, editorial staff, corresponding author, reviewers, and the publisher. The journal ensures that any unpublished work must not be used in Editor's, and reviewer's own research without the explicit written consent of the author(s).

Publication Decisions: The Chief Editor of the journal is responsible for deciding the publication or rejection of the submitted manuscript. The Chief Editor may take suggestion with other editors or reviewers in making decision.

Publisher: VB Foundation

CNS&E Editorial Board

Chief Editor

Prof. (Dr.) R K Kotnala,
Former Chairman NABL, Raja Ramanna Fellow DAE &
Chief Scientist, CSIR-National Physical Laboratory

Senior Editors

Prof. A C Pandey
Director, Inter University Accelerator Centre, New Delhi, India

Prof. K K Pant
Director IIT Roorkee, Uttarakhand, India

Prof. R K Sinha
Department of Applied Physics, DTU
Former Vice Chancellor, Gautam Buddha University and CSIR-CSIO Chandighar

Prof Sanjay Sharma
Director Indian Culture Study Centre-GBU
School of Information and Communication Technology Gautam Buddha University,
Greater Noida (UP)

Prof. Bhanooduth Lalljee,
President, Sustainable Agricultural Organisation ,External Professor at the Mauritius Institute of Education (MIE) and JSS Academy, Mauritius.

Editors

Dr. Indra Mani
Vice-Chancellor, Vasantrao Naik Marathwada Krishi Vidyapeeth, Maharashtra, India

Prof Nitin Puri
Executive Director-NIELIT, Patna Bihar
Professor-Delhi Technological University, Delhi

Prof Ajay Dhar
Associate Director, Academy of Scientific and Innovative Research, AcSIR, Ghaziabad-UP, India

Dr D S Rawal
Outstanding Scientist (Scientist-H) Solid State Physics Laboratory (SSPL), DRDO, Lucknow Road, Delhi

Prof Ambesh Dixit
Department of Physics, Indian Institute of Technology, Jodhpur, Rajasthan

Prof Deepak Pant
Department of Chemistry and Environmental Sciences Dean, School of Earth and Environmental Sciences; Head, Department of Environmental Science
Central University of Himachal Pradesh.

Prof Manoranjan Kar
Department of Physics, Indian Institute of Technology, Patna, Bihar

Dr A K Srivastava
Former Director, CSIR-Advanced Materials and Processes Research Institute, CSIR-AMPRI, Bhopal

Dr. S K Jha
Former Outstanding Scientist and Head, Radiation Protection Section (Nuclear Fuels) Health Physics Division & Professor, HBNI, Bhabha Atomic Research Centre, Mumbai.

Dr. Nasimuddin
Principal Scientist, Antenna and Optical Department, Institute for Infocomm Research; Agency for Science, Technology, and Research, Singapore.

Associate Editors

CNS&E Volume 3, Issue 1, June 2026

Table of contents:

Chief Editor's Message

Editorial

Prof R K Kotnala
FNASC, FIGU, FMSI
Chief Editor, Current Natural Sciences & Engineering, (CNS&E) Journal

DOI: https://doi.org/10.63015/kotnala.2026.3.1

Email: *chiefeditor@cnsejournals.org*

Future Generation & Storage of Green Energy: A Big Challenge? Hydroelectric Cells, Perovskite Solar Cells, and Supercapacitors: A Rescue for Earth's Sustainability!

Solar and hydroelectric cells are well-known green energy devices for generating electricity to achieve net carbon zero and Earth's sustainability. Hydroelectric cells have shown an overwhelming response by producing hydrogen through water splitting in different modes. Nevertheless, the supercapacitor's role in charge storage is also very important.

Widely recognized and validated revolutionary Hydroelectric Cell (HEC)—a paradigm-shifting green energy technology that achieves room-temperature water splitting without external energy, directly advancing the global pursuit of Net Zero Carbon and earth sustainability. It achieves room-temperature water splitting by using a nanoporous, oxygen-deficient ferrite (or metal oxide) attached to two electrodes, zinc & silver, to generate clean electricity without external energy. Hydroelectric Cell invention is embedded with fundamentally challenges the traditional limits of green energy, proving that ambient moisture and advanced material physics can generate clean electricity directly.

There is an urgent demand for highly efficient energy storage devices due to steep increase in the basic requirements of energy in the day today's routine. Supercapacitor based on Zinc Oxide being a cost-effective and environmentally friendly electrode, shows a promising future in this direction. However, its practical application is hindered by prevailing low electrical conductivity, which leads to poor electrochemical performance. To increase the energy storage capacity of ZnO, a recent study published in this issue innovated a Zinc Oxide/ Carbon Black (Zn/CB) nanocomposite electrode. The Zn/CB nanocomposite electrode exhibited a remarkable increase in specific capacitance compared to the pristine ZnO. It increased from 128 F/g (ZnO) to 375 F /g (Zn/CB) at a 10 mV/s scan rate. Moreover, the composite displays exceptional cyclic stability, showing 145% capacitance retention of 145% and coulombic retention of 94% after 3000 cycles @ 15 A/g. These interesting results demonstrate that integrating carbon black with zinc oxide substantially enhances its electrochemical performance, positioning the ZnO/CB nanocomposite electrode as a cost-effective, high-performance, nature-friendly electrode for future energy storage systems.

The breakthrough of utilizing water's spontaneous chemisorption followed by phyisorption on nano-porous metal oxide surfaces—while simultaneously synthesizing highly valuable biocompatible nanoproducts (nano-zinc hydroxide and hydrogen)—is a masterclass in elegant circular engineering. It is a massive contribution to the scientific community and a vital blueprint for India's sustainable future.

The Current Natural Sciences & Engineering Journal (CNS&E) moved forward with high expectations to facilitate novel ideas and technologies from the scientific community, aiming to provide people with a more comfortable and healthy life. To promote the welfare of Earth's sustainability and nature for sustainable life in a clean environment, the journal is facilitating the quick publication of new ideas and science-based manuscripts. In this direction, the CNS&E journal is a big platform to disseminate researchers' new approaches to ideas/innovations at a global level in a short time.

With a unique objective, the CNS&E journal aims to inspire future directions in interdisciplinary science research, with the sole purpose of creating impactful science & engineering knowledge and breakthrough innovation for the betterment of the world. Our passionate scientific teams of editors and reviewers have a solemn resolution to conform to fundamental principles of research objectivity, integrity, and ethical norms to promote knowledge generation and publication, in a more transparent and credible way, through far-reaching impacts on holistic scientific development. The CNS&E journal has already strived for global visibility during the last two years and engaged the scientific community worldwide for better dissemination of knowledge with a truly new science promotion.

Current Natural Sciences & Engineering
Volume 3, Issue 1, 2026, 919-927

Enhancing Electrochemical Performance of ZnO Nanocomposite by Integrating Carbon Black for Supercapacitor Electrode

Shubham Mural[1], Shweta Tanwar[1], Anjali[1], Nirbhay Singh[2], Ramesh Kumar[3], Anurag Gaur[1]*

[1]Department of Physics, Netaji Subhas University of Technology, New Delhi, India
[2]Department of Applied Physics, School of Engineering and Technology, Amity University Gwalior, Madhya Pradesh, India
[3]Department of Physics, Meerut Institute of Engineering and Technology, Meerut, India

Received date: 04/04/2026, Acceptance date: 18/06/2026

***DOI:* http://doi.org/10.63015/5cm-2501.3.1**

Corresponding author: anuragdph@gmail.com

Abstract

Driven by the rising energy consumption throughout the world, there is an urgent demand for highly efficient energy storage devices. Zinc Oxide, due to its cost-effective and environmentally friendly nature, shows a promising future in this direction. However, its practical application is hindered by its low electrical conductivity, leading to poor electrochemical performance. To increase the energy storage capacity of ZnO, this study designs a Zinc Oxide/ Carbon Black (Zn/CB) nanocomposite electrode. The Zn/CB nanocomposite electrode exhibited a remarkable increase in the specific capacitance (S_c) as compared to the pristine ZnO. It increased from 128 F g^{-1} (ZnO) to 375 F g^{-1} (Zn/CB) @ 10 mV s^{-1} scan rate. GCD analysis confirms this, showing an increase from 15 F g^{-1} (ZnO) to 183 F g^{-1} (Zn/CB) @ 4 A g^{-1}. Crucially, the composite displays exceptional cyclic stability by showing capacitance retention of 145% and coulombic retention of 94% after 3000 cycles @ 15 A g^{-1}. This finding demonstrates that the integration of carbon black with the Zinc Oxide substantially enhances its electrochemical performance, positioning the ZnO/CB nanocomposite electrode as a cost-effective, high-performance, nature-friendly electrode for energy storage systems.

Keywords: Carbon; Zinc Oxide; co-precipitation method; Hybrid supercapacitor.

1. Introduction

Rapid increase in the energy demands combined with the need for eco-friendly development has driven advances in the sustainable energy technologies [1], [2]. Energy resources are a vital and critical aspect of modern society, as they have been used for powering homes and businesses, fueling transportation, and industries. Traditionally, non-renewable resources like coal, fossil fuels, and oil have fulfilled the energy demands. As the need to save the planet has increased, there is a total shift in the energy sector. Sustainable energy resources are the necessity of the hour [3]. Energy storage systems play a critical role in making the sustainable energy resources feasible in day-to-day life [4], [5]. Electrochemical capacitors and batteries have become the leading option for energy storage applications [6]. Limitations of traditional carbon-based materials in the electrochemical performances led a path for the transition metal oxide (TMOs) materials to become highly desired candidates for energy storage applications [4], [7], [8].

Zinc Oxide (ZnO) stands out among TMOs as a highly capable energy storage material. It demonstrates excellent electrochemical activity, eco-friendliness, and ease of production [9], [10]. Despite these advantageous properties, ZnO supercapacitors face several significant challenges. Various composites of ZnO have been synthesized to overcome these shortcomings [7]. Recent advances in ZnO/Carbon composites have demonstrated that the carbon critically governs conductivity, ion transport, and cyclic stability in supercapacitor electrodes [11]. In ZnO/graphene systems, reduced graphene oxide (rGO) provides a high surface area and conductive network that enhances the charge collection. Microwave-assisted graphene-ZnO nanocomposites have reported capacitances of 146 F g^{-1}, while rGO/ZnO hybrids achieved ~260 F g^{-1} [12]. ZnO/CNT composites offer high-conductivity networks that facilitate rapid electron transport and mechanical robustness in flexible devices. More elaborate architectures, such as ZnO quantum dots/carbon/CNT, reach 185 F g^{-1} at 0.5 A g^{-1} current density and an all-solid-state asymmetric device delivering 23.6 Wh kg^{-1} energy density [13]. ZnO/Activated Carbon (ZnO/AC) composites present a cost-effective route with accessible porosity and good electrochemical reversibility. A ZnO/AC nanocomposite electrode showed 160 F g^{-1} specific capacitance for a 1:1 composition, with stable capacitance up to 5000 cycles [14]. Although ACs are economical and readily available, they often require higher mass loadings, which can limit rate capability [15]. Given this landscape, carbon black is used over CNTs or graphene because, while graphene and CNTs offer high performance, they are significantly more expensive and require complex processing. Carbon black is highly cost-effective and scalable. It is compatible with standard slurry mixing, achieving effective percolation, whereas the CNTs and graphene are 3 to 8 times more expensive and require specialized dispersion. Carbon black's percolation behaviour and conductivity support the formation of an efficient conductive network in composites at moderate loadings [16], [17].

This study reports the synthesis of pure ZnO and its composite with carbon black (Zn/CB) via the co-precipitation method. A systematic investigation of their structural, morphological, and electrochemical characteristics was carried out.

2. Experimental Section

2.1. Chemicals Utilized

Sodium hydroxide ($NaOH$), Zinc Nitrate hexahydrate ($Zn(NO_3)_2.6H_2O$) and carbon black (CB), all procured from Loba chemicals. Double-deionized water (DI) is used as a solvent for sample preparation.

2.2. Synthesis of the ZnO and ZnO/CB composite

Figure 1. Schematic depicting preparation of (a) ZnO, and (b) ZnO/CB

Zinc Oxide nanoparticles were fabricated via the co-precipitation route as shown in **Figure 1a**. Initially, 14.88 g of ($Zn(NO_3)_2.6H_2O$) was dissolved in 50 mL of distilled water under non-stop magnetic stirring at 600 rpm for 6 hours. The solution's pH was then adjusted to 8-10 by mixing 2-4 ($NaOH$) Pallets. After 6 hours of ageing, white precipitates were formed. Further washing and drying of the formed precipitates was done to collect the fine powder. To remove remaining moisture, the ZnO nanoparticles were dried at 60 °C for 24 hours in a vacuum oven. ZnO/CB nanocomposite were made by merging equal amounts (1:1) of ZnO and Commercial Carbon Black as depicted in **Figure 1b**.

2.3. Instruments used:

Powder X-ray diffraction (XRD) was performed to observe the crystallographic structure and phase purity of the prepared samples. The analysis utilized a D-8 X-ray diffractometer (Bruker, USA) with Cu Kα radiation, having a wavelength of approximately 1.5406 Å. The samples' morphological features were studied using a field-emission scanning electron microscope (FESEM) on a Zeiss Gemini SEM 500 (Carl Zeiss, Germany), operated at an accelerating voltage of 10 kV. Electrochemical properties of the electrode materials were assessed through Cyclic Voltammetry (CV) and Galvanostatic Charge-Discharge (GCD) using a SP-240 potentiostat (BioLogic Science). All electrochemical tests were directed in ambient conditions using a conventional three-electrode setup.

2.4. Electrode fabrication for electrochemistry

The working electrode for electrochemical analysis was fabricated using a standardized composition of 8:1:1 by weight. Initially, the active material, either ZnO or ZnO/CB nanocomposite, was weighed to constitute 8 wt.%, while polyvinylidene fluoride (PVDF) binder and conductive carbon black were incorporated at 1 wt.% each. These three components were homogenized using a mortar and pestle with N-methyl-2-pyrrolidone (NMP), thus forming a uniform slurry [18]. This slurry was evenly applied onto a 1×1 cm^2 area of nickel foam substrate (measuring 2×1 cm^2) functioning as the current collector. After coating, the electrodes were dried at 60°C for 2 hours to eliminate any remaining solvent.

3. Results and discussion

3.1. Crystal Structure investigation

The XRD patterns of pristine ZnO and ZnO/CB composite are depicted in **Figure 2**. The grey curve corresponds to the ZnO nanoparticle whereas the red curves correspond to the Zn/CB nanocomposite.

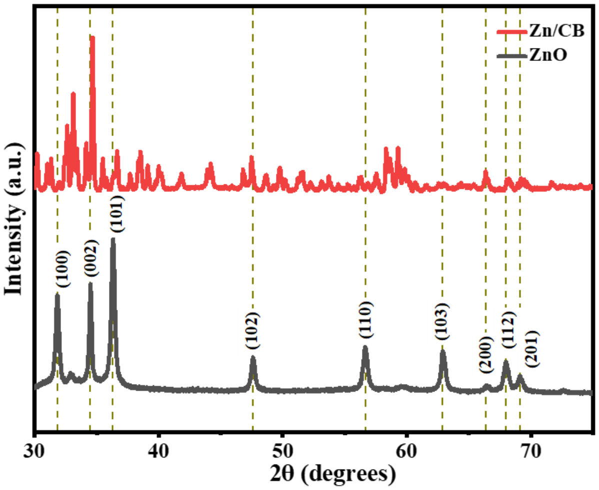

Figure 2. XRD curves of ZnO (Grey) and ZnO/CB (Red) sample.

The pristine ZnO sample exhibits distinct sharp and intense peaks at 2θ angles near 31.8°, 34.4°, 36.3°, 47.6°, 56.6°, 62.9°, 66.4°, 68°, and 69.1°, connects to (100), (002), (101), (102), (110), (103), (200), (112), and (201) crystal planes. From (JCPDS- 36-1451), it is confirmed that these are the peaks of the hexagonal ZnO structure [19]. Using the Debye-Scherrer equation applied of the prominent (101) peak, the average crystallite size of the pristine ZnO nanoparticles was calculated to be around 47nm. The ZnO/CB composite showed a noticeable decrease in the intensity of ZnO peaks along with slight broadening of the peaks. This broadening and decrease in peak intensity is due to the amorphous property of the Carbon Black component.

3.2. Morphology study using FESEM

The FESEM image of ZnO nanoparticles **(Figure 3a)** reveals a highly agglomerated microstructure. The material exhibits densely packed grains that form large, cauliflower like aggregates [20]. Whereas the FESEM image of ZnO/CB nanocomposite **(Figure 3b)** exhibits a heterogeneous and highly textured architecture. The ZnO/CB nanocomposite's structure appears more interconnected with increased surface roughness, suggesting a successful integration of the CB particles.

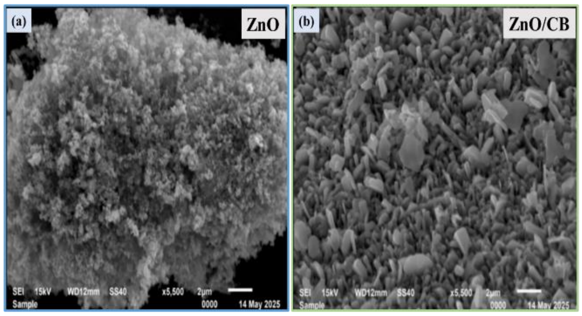

Figure 3. FESEM images (a) pure ZnO, and (b) ZnO/CB composite at two-micrometer scale.

Such an increase in granular morphology and textural complexity is generally favorable for electrochemical applications. It can facilitate improved electrolyte interaction and support enhanced charge storage performance as observed in the following electrochemical evaluation [21], [22].

3.3. Electrochemical behaviors study

Cyclic Voltammetry (CV) analysis revealed distinct redox peaks, attributable to oxidation and reduction processes, which align with the reports from previous studies on ZnO-based electrodes [23], [24]. In this setup, ZnO material was deposited onto the working electrode, while the Ag/AgCl (reference electrode) and Platinum (counter electrode) were used as other electrodes in a three-electrode configuration. 1M KOH was used as electrolyte and 0 V to 0.55 V was optimized as working potential window. CV curves at several scan rates (10 to 100 mV s^{-1}) for both ZnO and ZnO/CB samples are depicted in **Figure 4(a-b)**. ZnO electrode materials showed two distinct peaks at 0.31 and 0.5V. These oxidation and Redox peaks depicts that the charge storage mechanism is pseudocapacitance. These strong redox peaks are due to the K^+ ions intercalation/de-intercalation into the ZnO composite [25]. Upon incorporation of CB into ZnO, significant enhancements in the electrochemical behavior were observed in CV analysis. Graphically the area of the I-V curve increased significantly. The integration of Carbon Black changed the shape of the curve to quasi-rectangular with oxidation and reduction peaks around 0.35V and 0.5V. This indicates that the ZnO/CB composite comprises of both pseudocapacitance and electrochemical double-layer capacitance as the charge storage mechanism. As depicted in **Figure 4c**, when both materials were evaluated at a scan rate of 10 mV s^{-1}, the S_c of ZnO/CB almost reached 375 F g^{-1}, nearly three times more than the S_c of pristine ZnO (128 F g^{-1}), under same conditions. The S_c of the sample was estimated for different scan rates as shown in **Figure 4d**. Formula applied for calculating specific capacitance (S_c) [3] from the CV curves is:

$$S_c = \frac{\int i.dv}{m \times v \times \Delta V} \quad (F\,g^{-1}) \qquad (1)$$

Where area under CV curve is $\int i.dv$ (mA V), active mass loading (m) is 1 mg, scan rate is v (mV s^{-1}), and potential window ΔV (V).

GCD was performed to further describe the mechanism involved in charge accumulation and evaluate the capacitive performance of ZnO and ZnO/CB electrodes (**Figure 5**). Similar trends of the CV analysis is verified through the GCD curves also (**Figure 5a**). The discharging curve of the ZnO composite is nonlinear, which shows the pseudocapacitance as the charge storage mechanism. But in the ZnO/CB composite, after 0.35V, the discharge curve tends to be linear, showing the Electrochemical Double Layer capacitance component of charge storage. This clearly indicates the dual charge mechanism of the ZnO/CB (**Figure 5b)**.

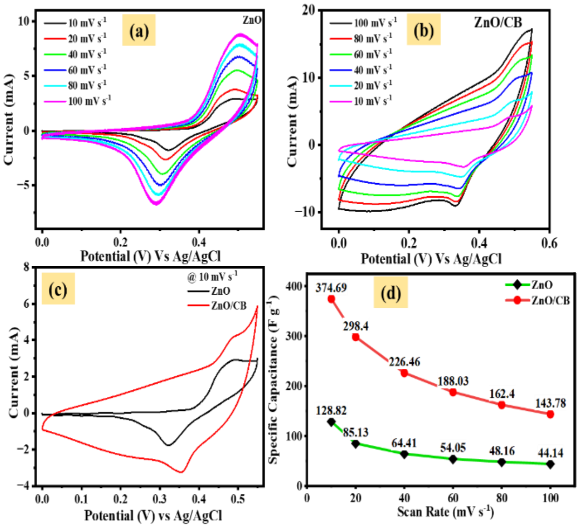

Figure 4. Cyclic voltammetry curves (a) ZnO, (b) Zn/CB, (c) evaluation at 10 mV s^{-1}, and (d) calculated S_c against scan rate for both prepared samples.

Figure 5c presents the comparative GCD profiles for the pristine ZnO, pure CB, and ZnO/CB nanocomposite electrodes, recorded at a current density of 4 A g^{-1}. The ZnO/CB nanocomposite exhibited the maximum discharge time, followed by pristine ZnO and finally the pure CB electrode, proving a genuine synergistic effect. The substantial prolongation of the discharge time confirms that the enhanced charge storage capacity arises from a cooperative interaction between the ZnO and the conductive CB network.

Figure 5(a-c) depicts the GCD curves for Zn/CB display noticeably prolonged charge time and discharge time at all tested current densities as compared to pristine ZnO, further implying a substantial improvement in charge storage capacity. The direct comparison at current density 4 A g^{-1}, highlights a dramatic improvement. In GCD analysis, the specific capacitance (S_c) [26] was determined by:

$$S_c = \frac{\Delta t \ \times I}{\Delta V \ \times m} \ (F \ g^{-1}) \qquad (2)$$

Here, discharge time is Δt (s), Current density is I (A g^{-1}), potential window is ΔV (V), and active mass loading is m. The maximum specific capacitance shown by the Zn/CB sample is 183 F g^{-1}, while ZnO shows 15 F g^{-1} @ 4 A g^{-1}.

The disparity between CV and GCD derived specific capacitance values can be attributed to the fundamentally different operational mechanisms of the two techniques. At low scan rate of 10 mV s^{-1}, there is ample time for electrolyte ions to diffuse deeply and bulk Faradaic reactions to occur, yielding higher capacitance. Whereas the lower GCD-derived values are due to the high current density of 4 A g^{-1}, the charge-discharge process does not have enough time for proper diffusion of the electrolyte ions, and only the outermost surface of the electrode participates in charge storage.

Long-term cycling **(Figure 5e)** was evaluated for ZnO/CB nanocomposite over 3,000 cycles at a current density of 15 A g^{-1}. Remarkably, the composite exhibited an excellent durability, with the specific capacitance actually increasing over every cycle, making the capacitance retention increase to 145%. It depicts that this electrode actually gets better as it operates. This increase is caused by the activation of the electrode. Initially, the electrolyte only interacts with outer surface of the electrode. However, the continuous charging and discharging acts as a driving force, slowly pushing the liquid electrolyte deeper into the electrode. This exposes previously inaccessible interior surface area and activates deeply embedded ZnO redox sites. The continuous integration of these fresh active sites counteracts any structural degradation and demonstrates exceptional capacity retention [27]. The coulombic efficiency improved from 87% to 94%, confirming the high reversibility and structural stability of the ZnO/CB electrode. Electrochemical Impedance Spectroscopy (EIS) was also performed on the ZnO/CB nanocomposite electrode. The resulting

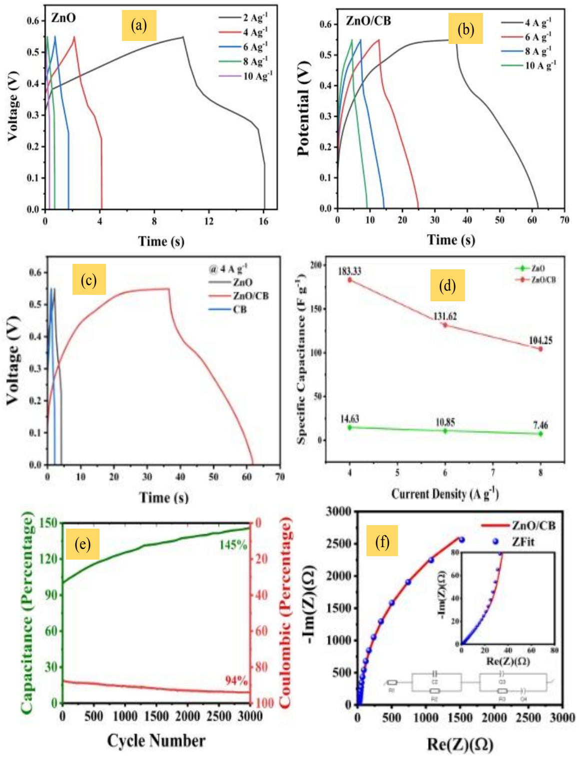

Figure 5. GCD curves: (a) ZnO, (b) ZnO/CB composite, (c) GCD of both ZnO and ZnO/CB 4 A g^{-1}, and (d) calculated S_c against current density for both prepared samples. (e) Capacitance retention and Coulombic retention over 3,000 cycles at 15 A g^{-1} of ZnO/CB composite. (f) Nyquist plot of ZnO/CB composite with equivalent fitted circuit.

Nyquist plot **(Figure 5f)** was fitted to an equivalent circuit. This composite demonstrates a notably low equivalent series resistance (R_s) of 1.1 Ω. Furthermore, the charge transfer resistance (R_{ct}) is restricted to a low value of 47 Ω. These low impedance values confirm that the integration of CB establishes a robust conductive network and facilitates rapid electron transport.

4. Conclusion

This study highlights a significant improvement in electrochemical performance achieved by incorporating carbon black into zinc oxide to form a Zn/CB nanocomposite. Pristine ZnO, while cost-effective and environmentally benign, suffers from low electrical conductivity, which limits its application as an efficient electrode material. The strategic inclusion of carbon black addresses this drawback establishing a highly conductive network within the composite, that significantly enhances the electron transportation. Electrochemical testing showed dual charge storing mechanism which increased S_c of 128 F g^{-1} for pristine ZnO to 375 F g^{-1} for ZnO/CB @ 10 mV s^{-1} scan rate and from 15 F g^{-1} for ZnO to 128 F g^{-1} for Zn/CB @ 4 A g^{-1} current density. This notable increase underscores the role of conductive additives in improving the overall charge storage performance of metal oxide-based materials. Furthermore, the simplicity and scalability of the synthesis method, coupled with the low cost of the components, position the ZnO/CB nanocomposite as a promising candidate for practical applications in energy storage. Overall, this work offers valuable insights into the design of efficient, low-cost, and environmentally sustainable electrode materials.

Acknowledgement

One of the authors, Shubham Mural, acknowledges Netaji Subhas University of Technology for the University Research Fellowship (URF).

References:

[1] K. Kumar *et al.*, “Exploring the Uncharted Territory: Future Generation Materials for Sustainable Energy Storage”, doi: 10.1051/e3sconf/202343001199.

[2] N. Kumar, S. Bin Kim, S. Y. Lee, and S. J. Park, “Recent Advanced Supercapacitor: A Review of Storage Mechanisms, Electrode Materials, Modification, and Perspectives,” *Nanomaterials*, vol. 12, no. 20, Oct. 2022, doi: 10.3390/NANO12203708,.

[3] S. Tanwar, A. Arya, A. Gaur, and A. L. Sharma, “Transition metal dichalcogenide (TMDs) electrodes for supercapacitors: a comprehensive review,” *Journal of Physics: Condensed Matter*, vol. 33, no. 30, p. 303002, Jun. 2021, doi: 10.1088/1361-648X/ABFB3C.

[4] S. Najib and E. Erdem, “Current progress achieved in novel materials for supercapacitor electrodes: mini review,” *Nanoscale Adv.*, vol. 1, no. 8, p. 2817, 2019, doi: 10.1039/C9NA00345B.

[5] Y. Wang and Y. Xia, “Recent progress in supercapacitors: From materials design to system construction,” *Advanced Materials*, vol. 25, no. 37, pp. 5336–5342, Oct. 2013, doi: 10.1002/ADMA.201301932,.

[6] M. Sharma and A. Gaur, “Designing of Carbon Nitride Supported $ZnCo_2O_4$

Hybrid Electrode for High-Performance Energy Storage Applications," *Sci. Rep.*, vol. 10, no. 1, pp. 1–9, Dec. 2020, doi: 10.1038/S41598-020-58925-4;SUBJMETA=4077,639,925;KWRD=ENERGY+SCIENCE+AND+TECHNOLOGY,NANOSCIENCE+AND+TECHNOLOGY.

[7] P. Pazhamalai, V. Krishnan, M. S. Mohamed Saleem, S. J. Kim, and H. W. Seo, "Investigating composite electrode materials of metal oxides for advanced energy storage applications," *Nano Converg.*, vol. 11, no. 1, p. 30, Dec. 2024, doi: 10.1186/S40580-024-00437-2.

[8] I. Shaheen, K. S. Ahmad, C. Zequine, R. K. Gupta, A. G. Thomas, and M. A. Malik, "Facile ZnO-based nanomaterial and its fabrication as a supercapacitor electrode: synthesis, characterization and electrochemical studies," *RSC Adv.*, vol. 11, no. 38, pp. 23374–23384, Jul. 2021, doi: 10.1039/D1RA04341B.

[9] I. Shaheen, K. S. Ahmad, C. Zequine, R. K. Gupta, A. G. Thomas, and M. A. Malik, "Facile ZnO-based nanomaterial and its fabrication as a supercapacitor electrode: synthesis, characterization and electrochemical studies," *RSC Adv.*, vol. 11, no. 38, pp. 23374–23384, Jul. 2021, doi: 10.1039/D1RA04341B.

[10] G. M. Di Mari, G. Mineo, G. Franzò, S. Mirabella, E. Bruno, and V. Strano, "Low-Cost, High-Yield ZnO Nanostars Synthesis for Pseudocapacitor Applications," *Nanomaterials*, vol. 12, no. 15, p. 2588, Aug. 2022, doi: 10.3390/NANO12152588/S1.

[11] C. Lefdhil, S. Polat, and H. Zengin, "Synthesis of Zinc Oxide Nanorods from Zinc Borate Precursor and Characterization of Supercapacitor Properties," *Nanomaterials 2023, Vol. 13, Page 2423*, vol. 13, no. 17, p. 2423, Aug. 2023, doi: 10.3390/NANO13172423.

[12] K. Yang, K. Cho, and S. Kim, "Effect of carbon black addition on thermal stability and capacitive performances of supercapacitors," *Sci. Rep.*, vol. 8, no. 1, p. 11989, Dec. 2018, doi: 10.1038/S41598-018-30507-5.

[13] K. Abdullin *et al.*, "Enhancing the Electrochemical Performance of ZnO-Co3O4 and Zn-Co-O Supercapacitor Electrodes Due to the In Situ Electrochemical Etching Process and the Formation of Co3O4 Nanoparticles," *Energies (Basel).*, vol. 17, no. 8, p. 1888, Apr. 2024, doi: 10.3390/EN17081888/S1.

[14] "XRD patterns of ZnO nanorods, Inside ZnO (PDF 36–1451)." Accessed: Jul. 21, 2025. [Online]. Available: https://plos.figshare.com/articles/figure/_XRD_patterns_of_ZnO_nanorods_Inside_ZnO_PDF_36_8211_1451_/826568?file=1246215

[15] P. P. Rani, "Synthesis of zinc oxide by co-precipitation method," *~ 45 ~ International Journal of Chemical Studies*, vol. 12, no. 6, pp. 45–49, 2024, Accessed: Jul. 21, 2025. [Online]. Available: https://www.chemijournal.com

[16] Y. C. Chang and C. C. Hsu, "Synergetic effect of carbon black as co-catalyst for enhanced visible-light photocatalytic activity and stability on ZnO nanoparticles," *Solid State Sci.*, vol. 107, p. 106366, Sep. 2020, doi: 10.1016/J.SOLIDSTATESCIENCES. 2020.106366.

[17] "Effect of ZnO Addition on Structural Properties of ZnO-PANi/Carbon Black Thin Films".

[18] I. Shaheen, K. Shahzad Ahmad, C. Zequine, R. K. Gupta, A. G. Thomas, and M. Azad Malik, "Facile ZnO-based nanomaterial and its fabrication as a supercapacitor electrode: synthesis, characterization and electrochemical studies," 2021, doi: 10.1039/d1ra04341b.

[19] S. Kumar, F. Ahmed, N. M. Shaalan, N. Arshi, S. Dalela, and K. H. Chae, "Influence of Fe Doping on the Electrochemical Performance of a ZnO-Nanostructure-Based Electrode for Supercapacitors," *Nanomaterials*, vol. 13, no. 15, p. 2222, Aug. 2023, doi: 10.3390/NANO13152222.

[20] K. Pradeeswari, A. Venkatesan, P. Pandi, K. Karthik, K. V. Hari Krishna, and R. Mohan Kumar, "Study on the electrochemical performance of ZnO nanoparticles synthesized via non-aqueous sol-gel route for supercapacitor applications," *Mater. Res. Express*, vol. 6, Aug. 2019, doi: 10.1088/2053-1591/ab3cae.

[21] S. Tanwar, N. Singh, and A. L. Sharma, "Structural and electrochemical performance of carbon coated molybdenum selenide nanocomposite for supercapacitor applications," *J. Energy Storage*, vol. 45, p. 103797, Jan. 2022, doi: 10.1016/J.EST.2021.103797.

Current Natural Sciences & Engineering
Volume 3, Issue 1, 2026, 928-945

Optimization of Lead-Free $CsSnCl_3$ Perovskite Solar Cells by Electron and Hole Transport Layer Property Modulation Utilizing SCAPS-1D

Yashika Agarwal[1], Saanvi Suri[1], Adit Kumar[1] and Nitish Saini[1*]

[1] *DPS International, Golf Course Extension Road, Sector 50, Gurgaon, 122018, India.*

Received date:14/04/2026, Acceptance date: 18/05/2026

***DOI:* http://doi.org/10.63015/1her-2502.3.1**

Corresponding author: nitish2593@gmail.com

Abstract

Photovoltaics are key to the realization of the United Nations Sustainable Development Goals, with over 60 percent of global electricity projected to be supplied by solar energy by 2050, however, traditional silicon solar cells have been associated with high cost of fabrication, energy content and the electronic waste. Although high-performing, with their ABX_3 crystal structure that allows them to absorb strongly, transfer charges efficiently, and tune their bandgaps, lead-based perovskite solar cells (PSCs) are toxic and lacks stability issues that limit their application on the parameter of sustainability. This prompts the design of lead-free perovskites, among which cesium tin chloride ($CsSnCl_3$) is non-toxic, has an appropriate bandgap (1.3 -1.8 eV, depending on the conditions of modelling the material and its defects), and better ambient stability. It is observed that the perovskites based on chloride tend to have larger intrinsic bandgaps (>2 eV), thus, the effective bandgap used in this paper represents parameters that were actually simulated and not necessarily actual experimental results. Using SCAPS-1D, an all-inorganic CBTS/$CsSnCl_3$/ZnO heterostructure is optimized. The power conversion efficiency of 16.95% was achieved due to optimization. Theoretical simulations predict efficiency under ideal conditions, however, practical values are often lower due to defects, interface losses, and fabrication constraints.

Keywords: Perovskite Solar Cell (PSC), Hole Transport Layer (HTL), Electron Transport Layer (ETL), Lead-free Perovskites, Power Conversion Efficiency (PCE).

1.Introduction

In the context of increasing world energy consumption, exhaustion of fossil fuels, and the ever-growing fear of carbon emission and climate change, the creation of renewable energy technologies has become more and more essential [1]. Among these, solar energy is unique in terms of its quantity and the ability to scale. Perovskite solar cells (PSCs) have been particularly of interest in this respect due to their remarkable optoelectronic characteristics, such as high absorption coefficients, tunable bandgaps, long carrier diffusion lengths, and high carrier mobility [2]. These strengths make the PSCs as promising alternatives to the existing silicon based technologies that are facing problems in costs and environmental effects. The perovskites include a very broad variety of materials, including organic-inorganic hybrids and totally inorganic compounds. Although efficiencies of hybrid perovskites can be very high, they tend to be affected by the problem of stability, in contrast to the case of inorganic variants of perovskite, e.g. Cs-based halides, where thermal and structural stability is generally much higher [3]. The direct bandgap of perovskite materials allows efficient photon absorption and electron–hole pair generation without phonon assistance, thereby reducing recombination losses and improving charge extraction [4]. Lead based perovskite solar cells are highly efficient, due to their excellent optical and electronic properties, with the PCE of these lead based cells increasing from a mere 3.8% to 25.8%. [5]. However, the toxicity of lead (Pb) poses an encumbrance for large scale production and implementation of solar technology due to its environmental concerns and impact on human health. [6]. Consequently, current literature has devoted efforts to discovering alternative materials for similar applications. Metal halide perovskites - commonly based on elements like tin (Sn), germanium (Ge), and bismuth (Bi) - are environmentally friendly materials as they consist of entirely inorganic components which allow for reduction in costs and toxicity. [7,8].

Of these, Sn-based perovskites are frequently studied due to their favourable optoelectronic characteristics and enhanced stability. Tin can be found in various oxidation states and structural phases, which affects the material performance. Specifically, $CsSnCl_3$ presents a viable alternative for lead based solar cells owing to its high absorption coefficient (α), favourable carrier mobility, and suitable bandgap for effective high efficiency solar cell applications. [9]. PSCs performance highly relies on device architecture and charge transport layers. Electron transport layers (ETLs), hole transport layers (HTLs) are important in terms of charge extraction, recombination suppression and energy level alignment [10]. PSCs are generally designed in n-i-p or p-i-n devices, with the n-i-p device providing flexibility to systematic optimisation of transport layers and device parameters [11]. Although $CsSnCl_3$ based PSCs hold promise, the research is still immature in comparison to lead-based systems like $FAPbI_3$ and $MAPbI_3$, leaving key performance mechanisms poorly understood [12]. The isolation of effects of interdependent parameters is often challenged by experimental approaches and this has led to the use of numerical simulation to systematically optimise device properties.

We use numerical simulations in this research to explore $CsSnCl_3$ based PSCs and determine the best heterostructure designs. Our analysis is aimed at maximising the performance of the device in terms of PCE, open-circuit voltage (VOC), short-circuit current density (JSC), and fill factor. Our results provide important design criteria, such as an optimal absorber thickness (~0.6 μm), high tolerance of ZnO ETL to defects and doping variations, and high sensitivity of defect density of the HTL (~10^{15} cm -3), which is critically sensitive to recombination and overall efficiency.

2. Solar cell configuration and simulation methodology

2.2 Numerical Simulation using SCAPS-1D

Numerical simulations were performed using the Solar Cell Capacitance Simulator (SCAPS-1D) [13], which is a well-developed one-dimensional device simulator developed at the University of Gent. SCAPS-1D allows for the simultaneous solution of the coupled Poisson equation and the electron/hole continuity equations under steady-state conditions, thus providing a rigorous description of charge carrier transport, photogeneration, and recombination processes in multilayer photovoltaic structures. This feature allows the accurate tuning of the material and device parameters like the thickness of the layers, band gap, electron affinity, carrier mobilities, doping concentration, defect densities (both bulk and interface), recombination rates, and contact work functions without spending money on experimental processing. The motion of charge carriers in a photovoltaic device is essentially controlled by the interaction of electrostatics, generation, transport and recombination phenomena, which are quantitatively expressed in terms of a set of semiconductor equations [14].

The essence of electrostatic analysis lies in Poisson's equation, in which the spatial distribution of the electric field E in the device is linked to the local charge density ρ:

$$\frac{dE}{dx} = -\frac{\rho}{\varepsilon_s} = -\frac{q}{\varepsilon_s}\left[p - n + N_D^+(x) - N_A^-(x) \pm N_{\text{def}}(x)\right] \quad , \quad (1)$$

Here, q denotes the elementary charge, ε_s is the dielectric permittivity of the semiconductor, n and p represent the free electron and hole concentrations respectively, and N_D^+, N_A^-, and N_{def} refer to the densities of ionized donor, acceptor, and charged defect states. This equation determines the internal electric field profile, which influences carrier drift and assists in the establishment of potential barriers or wells critical for charge separation. The transport of carriers is then described by the electron and hole continuity equations. These express charge conservation by balancing spatial variations in carrier current densities (j_n for electrons, j_p for holes) with generation and recombination processes:

$$\frac{\partial j_n}{\partial x} + G - U_n(n,p) = 0 \quad (2)$$

$$-\frac{\partial j_p}{\partial x} + G - U_p(n,p) = 0 \quad ,(3)$$

The generation of electron-hole pair under AM1.5G irradiation is represented by G recombination rates of electrons and holes are denoted by U_n and U_p respectively. These continuity equations facilitate charge conservation by ensuring that any spatial nonuniformities in current are compensated by local generation or loss of carriers, maintaining the systematic stability of the device over time.

One of the primary recombination mechanisms in semiconductors, especially in materials with defect or trap states, is modelled by the Shockley–Read–Hall (SRH) recombination formalism. The corresponding recombination rate R_{SRH} is quantified as:

$$R_{\text{SRH}} = \frac{np - n_i^2}{\tau_p(n + n_1) + \tau_n(p + p_1)} \quad ,(4)$$

where n_i denotes the intrinsic carrier concentration, n_1 and p_1 are characteristic carrier concentrations related to the defect energy levels, while parameters τ_n, τ_p represent the effective carrier lifetimes for electrons and holes respectively. This relation characterises the role of defect states as recombination centres for electron-hole annihilation, reducing the carrier population available for electrical conduction.

The carrier lifetimes (τ) themselves are determined by microscopic defect parameters:

$$\tau = \frac{1}{\sigma N_t v_{th}} \quad ,(5)$$

where σ is the defect capture cross-section, N_t describes the trap density, and v_{th} is the thermal velocity of the carriers. This expression forms a relationship between microscopic physical characteristics of defects (including their density and carrier capturing ability) and macroscopic device performance metrics like carrier lifetime and recombination rates.

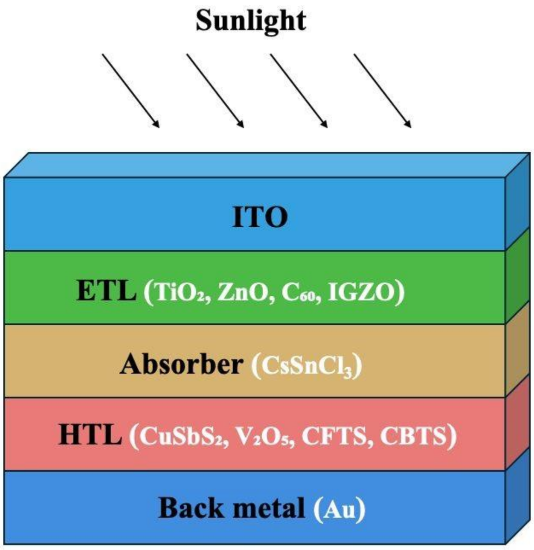

Figure 1: Schematic representation of the layer structure of the proposed $CsSnCl_3$-based perovskite solar cell architecture

2.2 $CsSnCl_3$-based Perovskite Solar Cell Structure and Energy Band Diagram

Numerical simulations of $CsSnCl_3$ perovskite solar cells (PSCs) were performed under a planar n-i-p cell geometry, in which the CsSnCl3 absorber acts as the intrinsic layer, while the hole transport layer (HTL) and electron transport layer (ETL) correspond to the p and n layers, respectively. Upon exposure to light, the CsSnCl3 perovskite material forms excitons, which disassociate effectively at the heterojunctions formed between the $CsSnCl_3$ and the HTL and ETL [13]. The electrons travel via the ETL to the ITO layer, while the holes are carried by the HTL to the Au back contact due to the presence of an electric field at the heterojunctions. The device structure used for the simulation is illustrated in Figure 1, consisting of the layered configuration ITO/ETL/$CsSnCl_3$/HTL/Au. From Figure 2 which presents the energy band alignment, it can be seen that both the electron and hole quasi-Fermi levels F_n and F_p are positioned closely to the conduction-band edge E_C and the valence-band edge, E_V within the absorber layer. While all the investigated ETLs show favourable valence-band alignment for efficient hole extraction, variations in their conduction-band edge positions lead to differences in electron extraction efficiency.

Specifically, the TiO_2, ZnO, and IGZO ETLs have comparable bandgaps, resulting in similar electron transport properties under identical simulation conditions as summarised in Table 3.

Table 1: Interface defect parameters used in the SCAPS-1D simulations

Interface	Defect Density N_{int} (cm^{-2})	Energy Level (eV)	Capture Cross-section σ (cm^2)
ETL/$CsSnCl_3$	1×10^{12}	Mid-gap	1×10^{-15}
$CsSnCl_3$/HTL	1×10^{12}	Mid-gap	1×10^{-15}

The front contact, ITO, possesses a work function of 4.0 eV, optimizing electron collection, whereas the Au back contact, with a work function of 5.1 eV, efficiently collects holes from the HTL. A comprehensive screening of multiple ETL and HTL materials was performed, testing 16 combinations with $CsSnCl_3$ fixed as the absorber. The combinations were evaluated based on photovoltaic metrics such as power conversion efficiency, open-circuit voltage, short-circuit current density, and fill factor.

The most promising ETL/HTL pairs were further optimized for thickness, doping, and defect densities. Interface defect densities at each heterojunction were also incorporated as summarized in Table 1. All simulations were conducted at a temperature of 300 K under AM1.5G solar illumination with an incident power density of 100 mW/cm^2, providing a realistic operational environment for the device performance assessment.

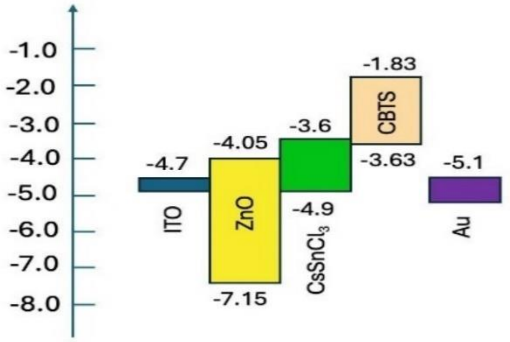

Figure 2: Simulated energy band alignment for the optimized solar cell as investigated

In addition to bulk defect densities, the effects of interface defect states at the ETL/perovskite and perovskite/HTL junctions were incorporated to accurately model recombination losses. Table 1 summarizes the interface defect densities, their energy levels, and capture cross-sections used in the simulations.

2.3 Simulation Strategy

The computational workflow comprised four sequential optimisation stages:

Stage 1: ETL/HTL combinatorial screening. All 16 ETL/HTL combinations were simulated for a fixed absorber configuration. Key photovoltaic parameters - namely power conversion efficiency (PCE), open-circuit voltage (V_{OC}), short-circuit current density (J_{SC}), and fill factor (FF) - were analysed, and the highest-performing ETL/HTL combination was selected.

Stage 2: Thickness optimization. Following the identification of the optimal ETL/HTL pair, the thicknesses of the ETL, absorber, and HTL were varied independently (ETL: 10–50 nm; absorber: 100–600 nm; HTL: 20–60 nm). The configuration yielding the highest PCE was retained.

Stage 3: ETL doping and defect tuning. The optimized thickness configuration was subsequently further evaluated by varying the ETL donor doping concentration (N_D, 10^{15}–10^{20} cm^{-3}) and ETL bulk defect density (N_t, 10^{10}–10^{15} cm^{-3}). The effects on V_{OC}, J_{SC}, FF, and PCE were monitored to identify optimal electronic properties.

Stage 4: HTL optimization. An identical doping/defect tuning process was applied to the HTL acceptor doping (N_A) and defect density.

Stage 5: Perovskite Optimization The donor density doping concentration and defect density of the perovskite $CsSnCl_3$ layer.

Table 2: Input parameters for the $CsSnCl_3$ absorber layer used in SCAPS-1D simulations

Parameter	Value
Thickness (nm)	500
Bandgap E_g (eV)	1.45
Electron affinity χ (eV)	4.10
Relative permittivity ε_r	15
Effective density of states in conduction band N_C (cm^{-3})	2.0×10^{18}
Effective density of states in valence band N_V (cm^{-3})	1.8×10^{19}
Electron mobility μ_n (cm^2/Vs)	20
Hole mobility μ_p (cm^2/Vs)	20
Intrinsic doping concentration N_i (cm^{-3})	1.0×10^{10}
Bulk defect density N_t (cm^{-3})	1.0×10^{14}
Capture cross-section σ (cm^2)	1.0×10^{-15}

2.4 Input Parameters

The key physical and electronic parameters of the $CsSnCl_3$ absorber used in the simulations are summarized in Table 2. These include the bandgap, electron affinity, dielectric constant, carrier mobilities, intrinsic doping levels, and defect densities, which critically influence the device performance Baseline parameters including bandgap, electron affinity, dielectric constant, carrier mobilities, doping concentrations, and defect densities were taken from experimental reports and validated simulations (Table 3).

3. Results and Discussion

3.1 Combinatorial Screening of Heterojunction Architectures

To identify an optimal device structure for $CsSnCl_3$ perovskite solar cells, we tried a combinatorial screening approach of 16 potential heterojunctions outlined in table. In this, different combinations of electron transport layers (ETLs) and hole transport layers (HTLs) were screened in a systematic way, keeping the $CsSnCl_3$ as absorber layer.

Four ETLs, IGZO, ZnO, TiO_2, and C_{60}, and four HTLs, CBTS, CFTS, V_2O_5, and $CuSbS_2$, were studied, which gave rise to 16 unique heterojunction configurations. All of the structures were simulated through the same boundary condition, interface parameter, and carrier transport property, enabling direct comparability of the V_{OC}, J_{SC}, FF, and η. The combinatorial screening serves to identify ETL/HTL pairs that maximise charge carrier extraction and minimise recombination losses as well as understand material dependent effects on device performance, including energy level alignment, carrier mobility, and interfacial recombination.

The results of the screening are summarised in Table 4. Of the configurations that were examined, the ZnO/$CsSnCl_3$/CBTS module yields the maximum balanced performance with V_{OC} = 0.7893 V, J_{SC} = 16.56 $mAcm^{-2}$, FF = 61.68%, and η = 7.15%. Devices constituting of V_2O_5 or $CuSbS_2$ as the HTL display prominent reductions in J_{SC} and efficiency which can be explained by increased interfacial recombination and inadequate energy alignment. Devices consisting of C_{60}-based ETLs exhibit moderate performance, primarily limited by the lower electron mobility of ZnO. Conversely, the TiO_2/$CsSnCl_3$/CBTS architecture achieves a similar efficiency of 7.14%, with a lower V_{OC} (0.5646 V) compensated by a higher J_{SC} (21.05 mA/cm^2). This demonstrates increased photon absorption but less favourable band alignment for effective voltage generation.

Table 3: Baseline input parameters for the Hole Transport Layer (HTL) and Electron Transport Layer (ETL) used in SCAPS-1D simulations.

Parameter		**HTL**				**ETL**		
	$CuSbS_2$	**V_2O_5**	**CFTS**	**CBTS**	**TiO_2**	**ZnO**	**C_{60}**	**IGZO**
Thickness (nm)	100	100	100	100	100	100	100	100
E_g (eV)	1.58	2.20	1.30	1.90	3.20	3.30	1.70	3.05
Electron affinity χ (eV)	4.20	4.00	3.30	3.60	4.00	4.00	3.90	4.16
ε_r	14.6	10	9	5.4	9	9	4.2	10
NC (cm^{-3})	2.0×10^{18}	9.2×10^{17}	2.2×10^{18}	2.2×10^{18}	2.0×10^{18}	3.7×10^{18}	8.0×10^{19}	5.0×10^{18}
NV (cm^{-3})	1.0×10^{19}	5.0×10^{18}	1.8×10^{19}	1.8×10^{19}	1.8×10^{19}	1.8×10^{19}	8.0×10^{19}	5.0×10^{18}
$v_{th,e}$ (cm/s)	1.0×10^{7}	1.0×10^{7}	1.0×10^{7}	1.0×10^{7}	1.0×10^{7}	1.0×10^{7}	1.0×10^{7}	1.0×10^{7}
$v_{th,h}$ (cm/s)	1.0×10^{7}	1.0×10^{7}	1.0×10^{7}	1.0×10^{7}	1.0×10^{7}	1.0×10^{7}	1.0×10^{7}	1.0×10^{7}
μ_n (cm^2/Vs)	49	3.2×10^{2}	21.98	30	20	100	8.0×10^{-2}	15
μ_h (cm^2/Vs)	49	4.0×10^{1}	21.98	10	10	25	3.5×10^{-3}	0.1
ND (cm^{-3})	0	0	0	0	9.0×10^{16}	1.0×10^{18}	1.0×10^{17}	1.0×10^{17}
NA (cm^{-3})	1.0×10^{18}	1.0×10^{18}	1.0×10^{18}	1.0×10^{18}	0	0	0	0
Nt (cm^{-3})	1.0×10^{15}	1.0×10^{15}	1.0×10^{15}	1.0×10^{15}	1.0×10^{15}	1.0×10^{15}	1.0×10^{15}	1.0×10^{15}

Table 4: Photovoltaic performance of different ETL/HTL combinations with $CsSnCl_3$ as the absorber.

Structure	**V_{OC} (V)**	**J_{SC} (mA/cm^2)**	**FF (%)**	**η (%)**
ZnO/$CsSnCl_3$/CBTS	0.7893	16.557014	61.68	7.15
ZnO/$CsSnCl_3$/CFTS	0.7902	16.565508	59.78	7.12
ZnO/$CsSnCl_3$/V_2O_5	0.5685	7.69E-01	63.34	0.28
ZnO/$CsSnCl_3$/$CuSbS_2$	0.4539	13.714259	45.75	2.85
TiO_2/$CsSnCl_3$/CBTS	0.5646	21.05632	60.03	7.14
TiO_2/$CsSnCl_3$/CFTS	0.5974	17.413918	56.00	5.83
TiO_2/$CsSnCl_3$/V_2O_5	0.3573	1.294983	63.32	0.29
TiO_2/$CsSnCl_3$/$CuSbS_2$	0.4492	14.276164	54.15	3.47
C_{60}/$CsSnCl_3$/CBTS	0.4224	25.076002	60.49	6.41
C_{60}/$CsSnCl_3$/CFTS	0.5730	19.916864	61.14	6.98
C_{60}/$CsSnCl_3$/V_2O_5	0.3405	6.61E-01	63.65	0.14
C_{60}/$CsSnCl_3$/$CuSbS_2$	0.2035	12.820296	53.92	1.41
IGZO/$CsSnCl_3$/CBTS	0.6642	19.304565	50.63	6.49
IGZO/$CsSnCl_3$/CFTS	0.7348	15.597707	59.31	6.80
IGZO/$CsSnCl_3$/V_2O_5	0.3698	2.260451	61.41	0.51
IGZO/$CsSnCl_3$/$CuSbS_2$	0.2006	11.306041	52.33	1.19

Promising J_{SC} values are obtained for C_{60} based modules, notably C_{60}/$CsSnCl_3$/CBTS (25.08 mA/cm^2), However, they are hindered by low V_{OC} (0.4224 V), which result in lower PCE outputs. IGZO-based configurations tend to be underperforming due to reduced FF and divergent energy levels, while V_2O_5 and $CuSbS_2$ HTLs exhibit extremely low efficiencies, arising from poor band alignment and high recombination rates.

These results indicate ZnO as the optimal ETL and CBTS as the optimal HTL, setting a baseline for further layer-specific optimization. The combinatorial approach efficiently informs experimental design, that resources be directed to optimize promising material combinations to obtain high-performance $CsSnCl_3$ heterojunction solar cells.

3.2 Thickness Optimisation Thickness optimisation of the Absorber Layer – $CsSnCl_3$

Here, perovskite absorber layer thickness optimisation within $CsSnCl_3$/ZnO heterojunction solar cell has been carried out in order to study absorber layer thickness-dependent performance parameter behavior. The property parameters of all the layers are held constant as specified in Tables 1 and 2, and flat-band ohmic contacts are assumed both at front and back sides. The $CsSnCl_3$ layer is tested with a doping concentration of × 1015 cm^{-3} while the ZnO ETL thickness is maintained at its optimal value. The thickness of the perovskite absorber layer is varied from 0.1 to 0.6 µm. Figure 4 depicts the photovoltaic parameter variation with absorber thickness. For thicknesses ranging from 0.1 to 0.3 µm, both V_{OC} and J_{SC} show a considerable rise. Values for V_{OC} increases from 0.6401 V to 0.7326 V, and J_{SC} increases from 16.34 to 22.47 mA cm^{-2}. This trend owes to the directly proportional relation between absorber thickness and photon absorption and carrier generation. However, beyond ~0.6 µm, recombination and transport losses begin to offset the gains from greater thickness, thereby diminishing efficiency improvements. Thicknesses exceeding 0.3 μm, provide declining but still useful returns. At 0.6 μm, V_{oc} is 0.7658 V, J_{sc} is 25.29 mA cm^{-2}, and FF increases from 68.37% at 0.1 μm to 78.87%, indicative of lower recombination and improved transport of carriers. These collective gains lead to a maximum efficiency of 15.27% at 0.6 μm, over twice the amount realized at 0.1 μm (7.15%). We observed that an increase in perovskite thickness from 0.6 μm would only give rise to marginal increases in performance due to likely recombination within the absorber and resistance losses within the ETL.

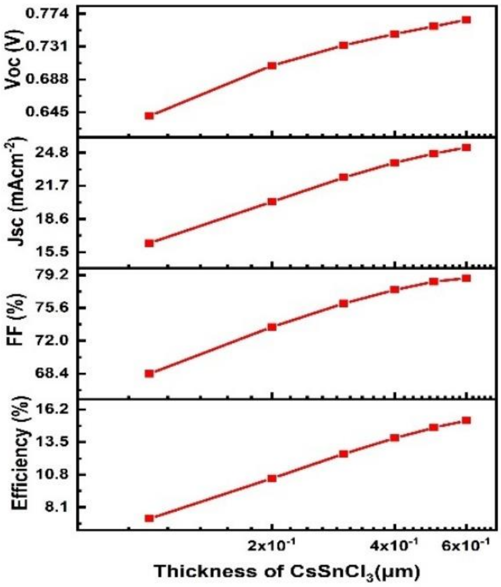

Figure 3: Variation of V_{oc}, J_{sc}, fill factor, and efficiency with thickness of the $CsSnCl_3$ layer

Consequently, forward in order to obtain optimal performance as tabulated in Table 5. An optimised 0.6 μm perovskite thickness is put for the $CsSnCl_3$/ZnO heterojunction solar cell,

3.3 Thickness optimisation of the Electron Transport Layer ZnO

Systematically, thickness optimisation of the ZnO electron transport layer (ETL) of the $CsSnCl_3$/ZnO/CBTS heterojunction solar cell has been studied. All other layer parameters, such as the perovskite absorber and the CBTS hole transport layer, remained as before, and flat-band ohmic contacts were used at each electrode. Thickness optimisation is paramount because each layer's performance hinges on balancing photo-generated carrier diffusion length, lifetime, and mobility, which determine charge separation across the heterojunction, recombination in the material concentration was maintained at 1×10^{15} cm^{-3}. The ZnO thickness was changed between 0.01 μm and 0.05 μm.

Figure 3 and Table 4 illustrate the device performance trends with varying thickness of the ZnO layer. From 0.01 μm to 0.03 μm, V_{oc} slightly rises from 0.7674 V to 0.7683 V due to enhanced electron blocking at the perovskite/HTL interface, minimizing the chances of hole back-transfer and maximizing built-in potential. J_{sc} shows only a very small drop from 25.496 mA cm^{-2} to 25.491 mA cm^{-2}, which suggests that the ZnO layer is still highly transparent over this range, with little optical loss and only slightly longer electron transport distances.

The fill factor (FF) decreases slightly from 79.87% to 79.66% over the same range, presumably a result of minute increases in series resistance created by thicker ETL. In spite of this, the PCE is maximized at 15.61% at 0.03 μm, the best compromise between enhanced voltage and containable resistive losses. While further increases in ZnO thickness, above 0.03 μm, lead to incremental losses in V_{oc} (to 0.7694 V at 0.05 μm) as well as larger FF losses (to 78.96%), smaller losses in J_{sc} (to 25.482 mA cm^{-2}) accompany these losses. This performance deterioration is due to higher series resistance as well as possible carrier recombination inside the ETL, which start restricting charge extraction efficiency.

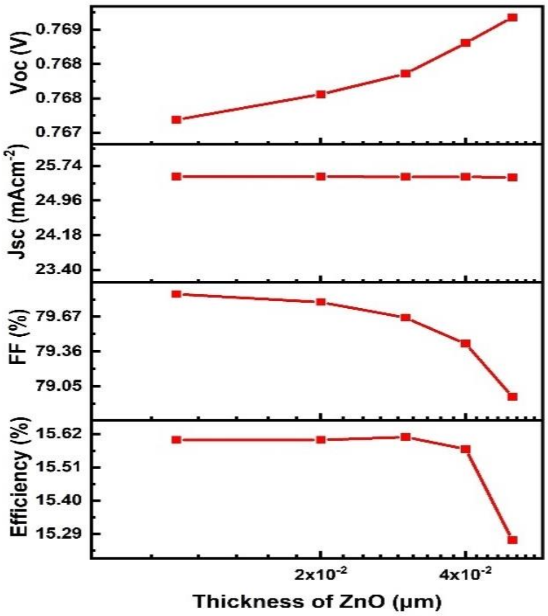

Figure 4: Variation of V_{oc}, J_{sc}, fill factor, and efficiency with thickness in the ZnO Layer.

The PCE drops to 15.27% at 0.05 μm, supporting the fact that thicker ETLs can degrade instead of improve overall performance.

On the basis of these findings, an optimised thickness of 0.03 μm for ZnO ETL is suggested since it provides the optimal compromise between the improved separation of charges, reduced resistive loss, and negligible optical attenuation and thus maximises efficiency in the $CsSnCl_3$/ZnO heterojunction solar cell.

Table 5: Thickness of perovskite absorber layer and photovoltaic performance.

Thickness (μm)	V_{oc} **(V)**	J_{sc} **(mA/cm^2)**	**FF (%)**	η **(%)**
0.1	0.6401	16.343394	68.37	7.15
0.2	0.7061	20.207083	73.5	10.49
0.3	0.7326	22.465648	76.07	12.52
0.4	0.7473	23.841284	77.56	13.82
0.5	0.7574	24.713258	78.46	14.69
0.6	0.7658	25.285758	78.87	15.27

3.4. *Thickness optimisation of the Hole Transport Layer (HTL) – CBTS*

The optimisation of the CBTS (Cu_2BaSnS_4) hole transport layer of the $CsSnCl_3$/CBTS heterojunction solar cell was conducted to evaluate the effect of varying the thickness of the HTL on the important performance parameters. The simulation parameters for all the layers were kept as stipulated in Tables 1 and 2, with flat-band ohmic contacts at both the front and rear interfaces. Perovskite absorber and ZnO ETL were both set at their respective optimised thickness levels, and the CBTS doping concentration was also maintained the same as the optimised setup. The CBTS thickness ranged from 0.02 μm to 0.06 μm.

Figure 5 and Table 6 present the ensuing photovoltaic trends. With increasing CBTS thickness from 0.02 μm to 0.04 μm, V_{oc} improved consistently from 0.7565 V to 0.7613 V. This is because improved interface coverage at the CBTS/perovskite junction decreases interfacial trap density and suppresses non-radiative recombination. J_{sc} improved from 25.005 mA cm^{-2} to 25.292 mA cm^{-2} at the same time which indicates more efficient hole extraction and less carrier backflow towards the absorber. Nonetheless, within the aforementioned range, the fill factor (FF) exhibited a slight reduction from 83.09% at a thickness of 0.02 μm to 81.3% at a thickness of 0.04 μm. This limited decrease can be attributed to increased series resistance with thicker HTL layers that compromises charge transport to some extent, despite improvement in interfacial quality. Hence, a modest but noticeable improvement was observed for the PCE, reaching 15.65% at the thickness of 0.04 μm that is, a balanced compromise among charge separation, transport efficiency, and resistive losses. However, when increasing from thicknesses more than 0.04 µm to 0.06 µm, there were some reductions in effectiveness. The open circuit voltage value was sustained but at an increased level of 0.7682 V while short circuit current density value was maintained at 25.492 mA cm^{-2} indicating further improvements in optical absorption and hole collection. FF fell more significantly to 79.72%, presumably a consequence of increasing cumulative resistive losses and enhanced probability of recombination in the thicker HTL. Consequently, PCE dropped marginally to 15.61% at 0.06 μm.

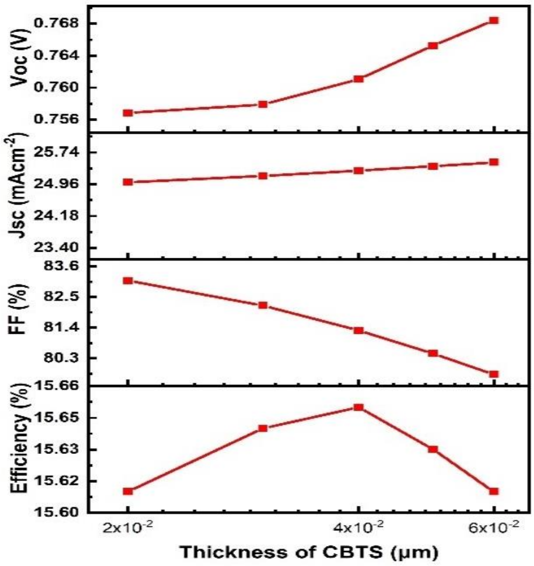

Figure 5: Variation of V_{oc}, J_{sc}, fill factor, and efficiency with thickness in the CBTS Layer.

Table 5: Thickness of perovskite absorber layer and photovoltaic performance.

Thickness (μm)	V_{oc} (V)	J_{sc} (mA/cm^2)	FF (%)	η (%)
0.01	0.7674	25.496096	79.87	15.60
0.02	0.7679	25.493633	79.80	15.60
0.03	0.7683	25.490602	79.66	15.61
0.04	0.7689	25.486913	79.43	15.57
0.05	0.7694	25.481651	78.96	15.27

As a whole, the results show that although incremental V_{oc} and J_{sc} improvements can be gained through increasing the thickness of the CBTS layer, the accompanying FF decrease counteracts these advantages. The optimal thickness of the CBTS layer is found to be 0.04 μm, where the device has its maximum simulated efficiency of 15.65% with a desirable balance between electrical and optical performance.

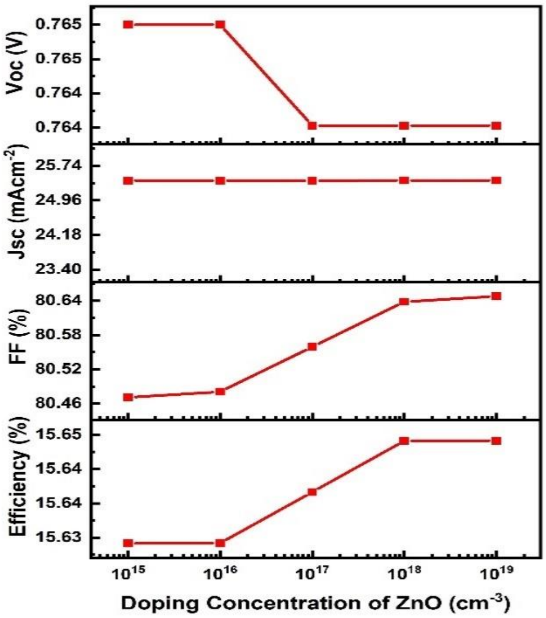

Figure 6: Variation of V_{oc}, J_{sc}, fill factor, and efficiency with doping concentration in the ZnO Layer.

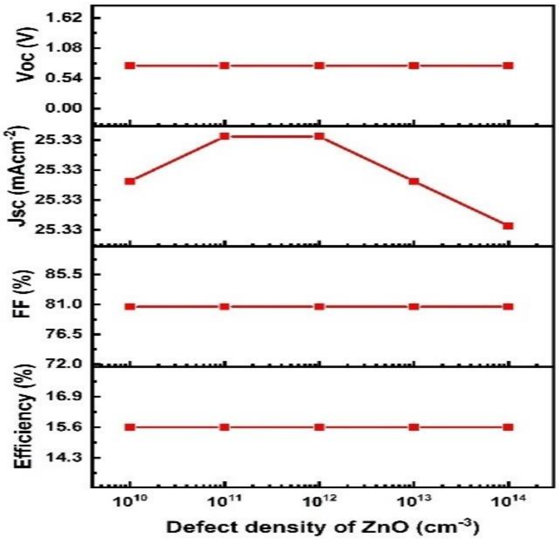

Figure 7: Variation of photovoltaic parameters — (a) open-circuit voltage (V_{oc}), (b) short-circuit current density (J_{sc}), (c) fill factor (FF), and (d) power conversion efficiency (PCE) as a function of ZnO electron transport layer doping concentration in the $CsSnCl_3$-based perovskite solar cell

.

Table 7: Thickness of CBTS HTL and photovoltaic performance.

Thickness (μm)	**V_{oc} (V)**	**J_{sc} (mA/cm^2)**	**FF (%)**	**η (%)**
0.02	0.7565	25.005136	83.09	15.61
0.03	0.7581	25.160604	82.19	15.64
0.04	0.7613	25.291760	81.30	15.65
0.05	0.7648	25.401410	80.47	15.63
0.06	0.7682	25.491622	79.72	15.61

3.4.1 ZnO Layer Doping and Defect Density Optimisation

The influence of defect density and donor density on the performance of the ZnO electron transport layer (ETL) in $CsSnCl_3$/ZnO/CBTS heterojunction solar cells was comprehensively examined. All the previously optimised parameters for the perovskite absorber (0.6 μm) and CBTS hole transport layer (0.04 μm) were kept constant, while having flat band ohmic contacts at both electrodes. Donor concentration of ZnO was changed from 1×10^{15} cm^{-3} to 1×10^{20} cm^{-3} and defect concentration was changed from 1×10^{10} cm^{-3} to 1×10^{15} cm^{-3} in order to investigate their impact on open-circuit voltage (V_{oc}), short-circuit current density (J_{sc}), fill factor (FF), and power conversion efficiency (η).

Figure 6 shows the donor density dependence of the performance parameters. The invariance of Voc with ZnO donor density indicates that the built-in electric field is primarily governed by band alignment rather than ETL doping, confirming that ZnO functions mainly as a charge transport layer rather than a junction-forming layer. J_{sc} varies very little (≈ 25.40–25.41 mA cm^{-2}), which means carrier generation and transport are not much affected by the donor concentration over this range. The fill factor (FF) is seen to improve marginally with an increase in donor density, implying that there is marginal improvement in charge transport but decreased resistive loss. This translates into the efficiency η improving minimally from 15.63% at 1×10^{15} cm^{-3} to 15.65% at 1×10^{20} cm^{-3}. There is also no influence from variations in defect density of ZnO in the cell performance. For example, the efficiency of ≈ 15.6%. This suggests that ZnO ETL is insensitive to intrinsic defect levels within the measured range, indicating strong the ranges considered for donor and defect densities, ZnO displays stable electronic properties, providing reliable V_{oc}, J_{sc}, and FF.

The results indicate that while J_{sc} remains nearly constant, FF and PCE increase with higher doping concentration, whereas V_{oc} slightly decreases beyond 10^{16} cm^{-3} slight variations in doping or defects will not significantly reduce device performance, making it easier to fabricate while retaining high efficiency carrier transport and low trap-assisted recombination in such conditions. In short, in V_{OC}, J_{SC}, and (FF) remain unchanged at around 0.7636 V, 25.33 mA cm^{-2}, and 80.65%, respectively, leading to an effectively constant The results show that J_{sc} remains nearly constant, while V_{oc}, FF, and PCE exhibit a sharp increase at doping concentrations above 10^{14} cm^{-3}.

3.4.2 *CBTS Layer Doping and Defect Density Optimization*

The effect of acceptor density and defect density on the performance of the CBTS hole transport layer (HTL) was systematically investigated while keeping all the previously optimized parameters such as $CsSnCl_3$

Table 8: Optimized performance parameters corresponding to ZnO donor and defect density

ZnO Parameter	V_{oc} **[V]**	J_{sc} **[mAcm^{-2}]**	**FF [%]**	η **[%]**
Donor Density 1×10^{15}	0.7648	25.40141	80.47	15.63
Donor Density 1×10^{16}	0.7647	25.40166	80.48	15.63
Donor Density 1×10^{17}	0.7644	25.40322	80.56	15.64
Donor Density 1×10^{18}	0.7640	25.40567	80.64	15.65
Donor Density 1×10^{19}	0.7638	25.40638	80.65	15.65
Donor Density 1×10^{20}	0.7637	25.40577	80.65	15.65
Defect Density 1×10^{10}	0.7636	25.33054	80.65	15.60
Defect Density 1×10^{11}	0.7636	25.33054	80.65	15.60
Defect Density 1×10^{12}	0.7636	25.33054	80.65	15.60
Defect Density 1×10^{13}	0.7636	25.33054	80.65	15.60
Defect Density 1×10^{14}	0.7636	25.33054	80.65	15.60
Defect Density 1×10^{15}	0.7636	25.33053	80.65	15.60

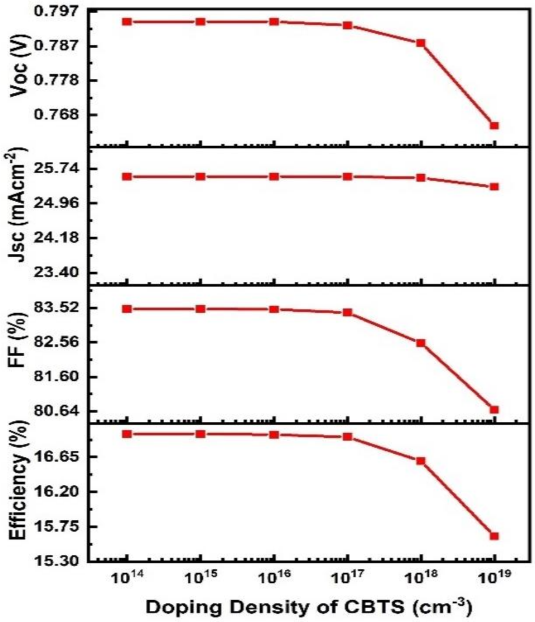

Figure 8: Variation of photovoltaic parameters — (a) open-circuit voltage (V_{oc}), (b) short circuit current density (J_{sc}), (c) fill factor (FF), and (d) power conversion efficiency (PCE) as a function of CBTS hole transport layer doping concentration in the $CsSnCl_3$-based perovskite solar cell.

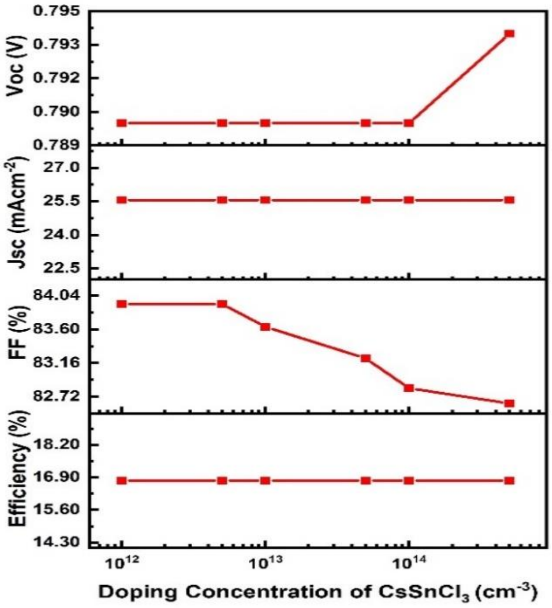

Figure 9: Influence of CBTS hole transport layer doping density on photovoltaic parameters — (a) open-circuit voltage (V_{oc}), (b) short-circuit current density (J_{sc}), (c) fill factor (FF), and (d) power conversion efficiency (PCE) — in $CsSnCl_3$-based perovskite solar cells.

perovskite thickness of 0.6 µm and ZnO ETL thickness of 0.03 µm. Flat-band ohmic contacts were assumed at both the electrodes. The density of acceptor in CBTS was tuned between 5 × 109 cm^{-3} to 5 × 1014 cm^{-3}, and defect density was tuned between 1 × 1014 cm^{-3} to 1 × 1019 cm^{-3} to analyse their effect on open-circuit voltage (Voc), short-circuit current density (Jsc), fill factor (FF), and power conversion efficiency (η). By comparison, the defect density of CBTS significantly impacts device performance. With the increase of defect density from 1 × 1014 cm^{-3} to 1 × 1015 cm^{-3}, Voc and FF rise to peaks of 0.7941 V and 83.49%, respectively. This is accompanied by an efficiency peak of 16.95%. The initial rise may be because of better band alignment and less interfacial trap-assisted recombination, leading to better charge extraction. However, after 1 × 1015 cm^{-3}, the performance decreases step by step: Voc reduces to 0.7651 V at 1 × 1019 cm^{-3}, FF reduces to 80.68%, and η returns to 15.63%. The observed performance degradation at higher defect densities confirms that trap-

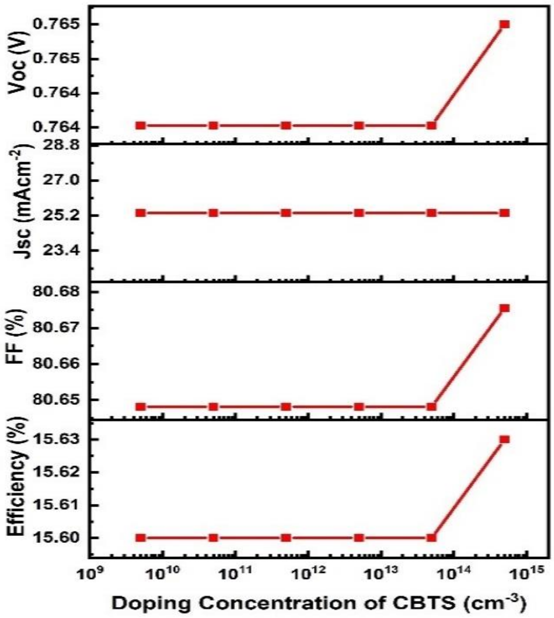

Figure 10: Effect of $CsSnCl_3$ absorber layer doping concentration on photovoltaic characteristics: (a) open-circuit voltage (V_{oc}), (b) short-circuit current density (J_{sc}), (c) fill factor (FF), and (d) power conversion efficiency (PCE).

assisted Shockley–Read–Hall recombination dominates in the HTL, reducing carrier lifetime and suppressing both fill factor and open-circuit voltage. Surprisingly, Jsc is quite stable (~ 25.33–25.56 $\mathrm{mAcm^{-2}}$) across the entire defect density range, suggesting that the density of photogenerated carriers is not appreciably influenced.

The findings show that although the density of CBTS acceptors affects the performance of the device to a small extent, defect density becomes the major parameter for controlling Voc, FF, and efficiency. An optimal defect density of 1×10^{15} $\mathrm{cm^{-3}}$ maximises efficient hole transport and reduces recombination contributing to the greater efficiency. Therefore, this emphasises the significance of the interface and bulk defect engineering of HTLs in the fabrication of perovskite solar cells. Thus, keeping defect density within the optimal value range is crucial for achieving high-performing $CsSnCl_3$/ZnO/CBTS heterojunction solar cells. An increase in doping concentration above 1×10^{13} $\mathrm{cm^{-3}}$ leads to a significant rise in V_{oc}, while J_{sc} and PCE are practically unaffected by the change in doping level. The fill factor shows a monotonic decrease with increasing doping concentration levels.

3.5 Perovskite Layer Doping and Defect Density Optimization

The present subsection considers the impact of acceptor density and defect density on the performance of the $CsSnCl_3$ perovskite in the $CsSnCl_3$/ZnO/CBTS solar cell. All the previously optimised parameters for the ZnO ETL and CBTS HTL are kept constant. The thickness of the perovskite absorber layer is constant at 0.6μm, with flat-band ohmic contacts existing at every electrode junction. Acceptor concentration is varied between 1×10^{12} $\mathrm{cm^{-3}}$ to 5×10^{14} $\mathrm{cm^{-3}}$, and defect concentration is varied between 1×10^{10} $\mathrm{cm^{-3}}$ to 1×10^{15} $\mathrm{cm^{-3}}$. The impact of variations in acceptor density on open circuit voltage (V_{oc}), short-circuit current density (J_{sc}), fill factor (FF), and total power conversion efficiency (η) is investigated. According to Figure **10**, as acceptor concentration rises from 1×10^{12} $\mathrm{cm^{-3}}$ to 5×10^{14} $\mathrm{cm^{-3}}$, open circuit voltage also increases from 0.7897V to 0.7942V respectively. This phenomenon can be associated with improved internal electric field strength due to higher doping concentrations, leading to higher efficiency in separating charges at the perovskite/ZnO interface. At the same time, no significant change is observed for J_{sc} which remains almost constant at ~ 25.56 mA $\mathrm{cm^{-2}}$, suggesting that photogeneration rate and carrier extraction are insensitive to variations in acceptor density over this range. A slight reduction in FF is found, ranging between 83.93% and 82.63%, which can be attributed to increased series resistance and reduced carrier mobility that accompany higher doping levels. Consequently, η remains constant at ~ 16.77%, highlighting that moderate acceptor density tuning can successfully balance the trade-off between high open circuit voltage and high recombination losses, thus ensuring stable overall device performance. Increasing defect density above 10^{13} $\mathrm{cm^{-3}}$ results in a sharp increase in V_{oc}, while J_{sc} remains relatively constant. FF and PCE exhibit a notable decline at higher defect densities mainly enhances V_{oc} without negatively affecting J_{sc} or FF. This proves that $CsSnCl_3$ layers are endowed with adequate intrinsic hole conductivity for effective carrier transport even under lower concentrations of doping. The identified defect density of the $CsSnCl_3$ layer significantly influences the performance, as shown in Figure 11. At defect densities ranging from low (1×10^{10}–1×10^{13} $\mathrm{cm^{-3}}$), V_{oc} is considerable (~ 0.7942V), J_{sc} does not change much (~ 25.56$\mathrm{mAcm^{-2}}$), and FF is around 83.4–83.5%, resulting in maximum efficiency of 16.95%

Table 9: Optimum performance parameters of CBTS acceptor and defect densities

CBTS Parameter	V_{oc} **[V]**	J**sc [mAcm**$^{-2}$**]**	**FF [%]**	η **[%]**
Acceptor Density 5 × 10^{9}	0.7636	25.33054	80.65	15.60
Acceptor Density 5 × 10^{10}	0.7636	25.33054	80.65	15.60
Acceptor Density 5 × 10^{11}	0.7636	25.33054	80.65	15.60
Acceptor Density 5 × 10^{12}	0.7636	25.33052	80.65	15.60
Acceptor Density 5 × 10^{13}	0.7637	25.33038	80.65	15.60
Acceptor Density 5 × 10^{14}	0.7651	25.32889	80.68	15.63
Defect Density 1 × 10^{14}	0.7941	25.55971	83.49	16.95
Defect Density 1 × 10^{15}	0.7941	25.55969	83.49	16.95
Defect Density 1 × 10^{16}	0.7940	25.55942	83.48	16.94
Defect Density 1 × 10^{17}	0.7934	25.55677	83.39	16.91
Defect Density 1 × 10^{18}	0.7878	25.53094	82.54	16.60
Defect Density 1 × 10^{19}	0.7651	25.32889	80.68	15.63

This indicates very little non-radiative recombination and effective carrier extraction. However, at high defect concentrations, especially 1 × 10^{15} cm^{-3}, FF dramatically decreases to 76.73%, with η also decreasing to 15.62%, even when V_{oc} is slightly increased to 0.8013V. This decrease is caused by increased trap-assisted non-radiative recombination that raises carrier loss and caps extraction efficiency at contacts. J_{sc} likewise exhibits a small drop, role. indicating smaller effective carrier collection. Hence, defect density is an important limiting factor in high-efficiency perovskite solar cells, with defect passivation strategies playing a vital role. These ranges ensure a balance between enhanced V_{oc} and high FF while minimising recombination losses, resulting in optimal efficiency of ~ 16.95%. The results show that though V_{oc} can be slightly improved through enhanced acceptor density, FF and η are mostly influenced by the density of defects. The utilisation of perovskite layers with low defect density (< 1×10^{14} cm^{-3}) is a key factor necessary for ensuring efficient carrier transport and maximum efficiency. The results show the need for high accuracy in material quality control and effective defect passivation in CsSnCl$_3$-based perovskite solar cells.

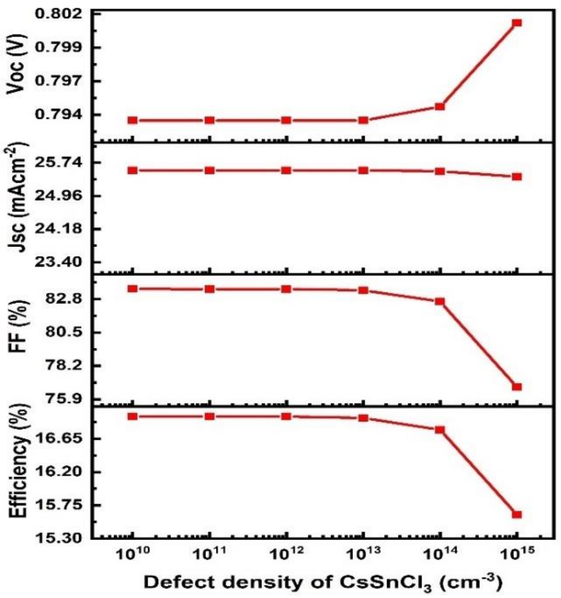

Figure 11: Influence of CsSnCl$_3$ absorber layer defect density on photovoltaic performance parameters V_{oc}, J_{sc}, FF, and PCE.

3.6 *Optimised Device Parameters and Interface Properties*

Despite being more efficient than most experimentally determined efficiencies of $CsSnCl_3$-based solar cells, it represents a theoretical maximum obtained under optimized and defect-minimized simulation conditions. In practical scenarios, factors such as interface imperfections, material instability, and fabrication constraints are expected to reduce achievable efficiencies.

These findings contribute to the advancement of lead free perovskite based solar cell development and computational photovoltaic modelling for a more sustainable future. Interface defect characteristics for the heterojunctions are summarized in Table 11. The optimized interface properties and layer parameters as a whole support the superior performance of the device. The ZnO ETL facilitates effective electron extraction and reduces recombination due to its low defect concentration and high electron mobility. The $CsSnCl_3$ perovskite absorber has strong absorption in the optical range, with an acceptor density that is well controlled and very few intrinsic defects, thus improving carrier lifetime and diffusion length. In the meantime, the CBTS HTL ensures effective hole transport and extraction while minimizing recombination at the perovskite/HTL interface. In addition, the interface defect densities are minimized to 1×10^{10} cm^{-3}, successfully avoiding trap-assisted recombination at the heterojunctions.

This optimisation of layer thickness, band alignment, carrier mobility, doping concentration, and defect densities leads to an optimised trade-off among V_{oc}, J_{sc}, and FF, resulting in a power conversion efficiency of 16.95%. The results highlight the need for accurate material and interface engineering for the realization of high-performance perovskite-based heterojunction solar cells. In summary, our work optimised lead-free $CsSnCl_3$ solar cells with a *n-i-p* heterostructure systematically using SCAPS-1D for a wide range of possible electron transport layers (ETLs) and hole transport layers (HTLs). A range of heterostructures within the ITO/ETL/$CsSnCl_3$/HTL/Au architecture were assessed and the most efficient module from 16 possible combinations with TiO_2, ZnO, C_{60}, and IGZO as ETLs and $CuSbS_2$, V_2O_5, CFTS, and CBTS as HTLs was optimised to identify structures yielding the highest performance. This research exhibits the potential of Pb-free $CsSnCl_3$ perovskite as an absorber layer for highly efficient PSCs. The optimisation of the PSC heterostructure by SCAPS-1D numerical simulation software showed that the combination of ZnO as electron transport layer, and CBTS as hole transport layer gave the highest PCE of 16.95%. To contextualize the obtained results, previously reported studies on tin-based and chloride perovskite solar cells typically demonstrate efficiencies in the range of ~5–12% in simulation and generally lower in experimental implementations [7,9,13]. The higher efficiency achieved in this work is attributed to systematic multi-parameter optimization, including minimized interface defect densities (~10^{10} cm^{-3}) and idealized band alignment. Therefore, the present results should be interpreted as a theoretical performance ceiling rather than a directly achievable experimental benchmark.

Table 10: Key material parameters of each functional layer.

Layer Parameter	**ZnO**	**$CsSnCl_3$**	**CBTS**
Thickness (μm)	0.027	0.646	0.05
Bandgap (eV)	2.527	1.558	1.4
Electron Affinity (eV)	3.5	3.8	3.65
Dielectric Permittivity	3	15.4	5.4
CB Effective DOS (cm^{-3})	3.7×10^{18}	1×10^{19}	2.2×10^{18}
VB Effective DOS (cm^{-3})	1.8×10^{19}	1×10^{19}	1.8×10^{19}
Electron Thermal Velocity (cm s^{-1})	1×10^{7}	1×10^{7}	1×10^{7}
Hole Thermal Velocity (cm s^{-1})	1×10^{7}	1×10^{7}	1×10^{7}
Electron Mobility (cm^2 V^{-1} s^{-1})	100	2	30
Hole Mobility (cm^2 V^{-1} s^{-1})	25	2	10
Shallow Donor Density N_D (cm^{-3})	1×10^{22}	0	0
Shallow Acceptor Density N_A (cm^{-3})	0	9×10^{14}	5.5×10^{14}
Defect Density (cm^{-3})	1×10^{10}	9×10^{10}	1×10^{10}

Table 11: Interface defect characteristics for the heterojunctions

Interface	**Electron Capture Cross-Section (cm^2)**	**Hole Capture Cross-Section (cm^2)**	**Energy w.r.t Reference (eV)**	**Defect Density (cm^{-3})**
CBTS /$CsSnCl_3$	$1x10^{-19}$	$1x10^{-19}$	0.6	$1x10^{10}$
$CsSnCl_3$ / ZnO	$1x10^{-19}$	$1x10^{-19}$	0.6	$1x10^{10}$

4 Conclusion

In conclusion, this study systematically optimised lead-free $CsSnCl_3$ solar cells with a *n-ip* heterostructure using SCAPS-1D for a diverse selection of potential electron transport layers (ETLs) and hole transport layers (HTLs). A range of heterostructures within the ITO/ETL/$CsSnCl_3$/HTL/Au architecture were assessed, and the most efficient module from 16 possible combinations with TiO_2, ZnO, C_{60}, and IGZO as ETLs and $CuSbS_2$, V_2O_5, CFTS, and CBTS as HTLs was optimised to identify structures yielding the highest performance. This study demonstrates the remarkable potential of lead-free $CsSnCl_3$ perovskite as an absorber layer for high-efficiency PSCs. Optimisation of the PSC heterostructure using SCAPS-1D numerical simulation software revealed that the combination of ZnO as the electron transport layer and CBTS as the hole transport layer resulted in the highest PCE of 16.95%. Furthermore, the influence of carrier density, defect density, and thickness of each layer on the overall module performance was evaluated. The results showcased that absorber defect density and acceptor density had no notable impact on PV efficiency, while absorber thickness had a significant impact on all 52 simulated modules of the chosen heterostructure. The initial device structure ITO/ZnO/$CsSnCl_3$/CBTS/Au yielded an efficiency of 7.15%. Optimisations led to an increase in efficiency 16.95% with a V_{oc} of 0.8 V, J_{sc} of 25.55 mA/cm^2, and FF of 82.89%. Additionally, this study establishes transferable design principles and guidelines for module fabrication, emphasizing the key role played by the defect density in HTL in limiting the performance, the indifference of the ETL, and the crucial role of absorber thickness. These findings provide a generalized framework for optimizing future lead-free perovskite solar cells beyond the specific ZnO/CBTS configuration.

Conflict of Interest:

There is no conflict to declare.

References

[1] JOHN BONGAARTS. “IPCC, 2023: Climate Change 2023: Synthesis Report. IPCC, 184 p., doi: https://doi.org/10.59327/IPCC/AR6-9789291691647”. In: *Population and Development Review* 50.2 (May 2024), pp. 577–580. issn: 1728-4457. doi: http://dx.doi.org/10.1111/padr.12632.

[2] Md Helal Miah et al. “Band gap tuning of perovskite solar cells for enhancing the efficiency and stability: issues and prospects”. *RSC Adv.* 14.23 (May 2024), pp. 15876–15906.

[3] Yu Zhang, Huan-Ping Zhou, and College of Engineering, Peking University, Beijing 100871, China. “Intrinsic stability of organic-inorganic hybrid perovskite”. *Wuli Xuebao* 68.15 (2019), p. 158804.

[4] Minhee Kim and Jinhyun Kim. “Recent research trends in inorganic charge transport materials for next-generation perovskite solar cells”. *Renew. Sustain. Energy Rev.* 219.115835 (Sept. 2025), p. 115835.

[5] Saikumar Nair and Jignasa V Gohel. “A study on optoelectronic performance of perovskite solar cell under different stress testing conditions”. Opt. Mater. (Amst.) 109.110377 (Nov. 2020), p. 110377.

[6] Zhiguo Zhang et al. “The importance of elemental lead to perovskites photovoltaics”. *Chemistry of Inorganic Materials* 1.100017 (Dec. 2023), p. 100017.

[7] Okba Saidani, Abderrahim Yousfi, and Girija Shankar Sahoo. “Numerical investigation of $CsSnCI_3$ perovskite solar cells utilizing WS_2 and $CuSbS_2$ transport layers for enhanced efficiency beyond 24%”. *Phys. Status Solidi (A)* 222.13 (July 2025).

[8] Teneng Assah Mbanga et al. “Charge carrier mobility and the recombination processes within a bulk heterojunction organic solar cell exhibiting disordered hopping”. *J. Ren. Energies* 272 (Dec. 2024).

[9] Eli Danladi et al. “20.730% highly efficient lead-free $CsSnI_3$-based perovskite solar cells with various charge transport materials: a SCAPS-1D study”. Multiscale Multidiscip. *Model. Exp. Des.* 8.1 (Jan. 2025).

[10] George G Njema, Joshua K Kibet, and Silas M Ngari. “A review of interface engineering characteristics for high performance perovskite solar cells”. *Measurement: Energy* 2.100005 (June 2024), p. 100005.

[11] Thibault Lemercier et al. “A comparison of the structure and properties of opaque and semi-transparent NIP/PIN-type scalable perovskite solar cells”. *Energies* 13.15 (July 2020), p. 3794.

[12] Zhiguo Zhang et al. “The importance of elemental lead to perovskites photovoltaics”. *Chemistry of Inorganic Materials* 1.100017 (Dec. 2023), p. 100017.

[13] Okba Saidani, Abderrahim Yousfi, and Girija Shankar Sahoo. “Numerical investigation of $CsSnCI_3$ perovskite solar cells utilizing WS_2 and $CuSbS_2$ transport layers for enhanced efficiency beyond 24%”. *Phys. Status Solidi (A)* 222.13 (July 2025)

[14] Teneng Assah Mbanga et al. “Charge carrier mobility and the recombination processes within a bulk heterojunction organic solar cell exhibiting disordered hopping”. J. Ren. Energies 27.2 (Dec. 2024).

Current Natural Sciences & Engineering
Volume 3, Issue 1, 2026, 946-953

Analysis of Effects of Different Loads on Diversity Parameters of a 4-port Multiband MIMO Antenna

Shailesh[1], Abhishek Kumar[1], Jyotsna Gaur[1], Amit Birwal[1], and Kamlesh Patel*[1]

Department of Electronic Science, University of Delhi South Campus, New Delhi-110021, India

Received date:30/04/2026, Acceptance date: 17/06/2026

DOI: http://doi.org/10.63015/8ms-2504.3.1

**Corresponding author: : kpatel@south.du.ac.in*

Abstract

This work investigates the effects of different loads on the diversity parameters of a multiband multiple-input multiple-output (MIMO) antenna. The unused ports of a 4-port multiband MIMO antenna are terminated with a matched load, an open load, or a short load when exciting one or two ports. The diversity parameters of MIMO antenna, such as Envelope Correlation Coefficient (ECC), Diversity Gain (DG), Total Active Reflection Coefficient (TARC), and Mean Effective Gain (MEG), are calculated using S-parameters. The maximum ECC values are 0.311, 0.314, and 0.302, and the minimum TARC values are -8.272 dB, -8.223 dB, and -8.035 dB, respectively, in the operating bands for these three loads. The DG is approximately 10 dB, and the MEG ratios are within ±3 dB across 4-6 GHz for the three different loads. Generally, the open load shows weak participation, while the short load offers strong coupling and severe diversity degradation. In the present study, the effects of these different loads are found to be negligible on the diversity parameters of the multiband MIMO antenna.

Keywords: S-parameters, MIMO Antenna, Diversity parameters, Multiband, System performance.

1. Introduction

In practice, each port of a Multiple-Input Multiple-Output (MIMO) antenna system is not isolated. It is connected to RF front-end circuits, matching networks, active components (LNAs, PAs, switches), etc. These introduce different load impedances, which are not always perfect 50 Ω. In real scenarios, instead of assuming all ports are perfectly matched, one should study the MIMO antenna performances with matched loads (50 Ω), mismatched loads, and open/short conditions to assess the reliability of the MIMO system. Most reported MIMO antennas assume that all inactive ports are terminated with a standard matched load and evaluate performance under ideal excitation conditions [1] [2] [3] [4] [5] [6]. However, in practical scenarios such as switching networks, reconfigurable systems, or fault conditions, antennas may experience open-circuit, short-circuit, or mismatched load states. The influence of these non-ideal terminations on key MIMO performance parameters, such as envelope correlation coefficient (ECC), diversity gain (DG), mean effective gain (MEG), and total active reflection coefficient (TARC), has not been systematically investigated in existing literature. Therefore, a clear research gap exists in analyzing and comparing MIMO antenna performance under matched load, open-circuit, and short-circuit conditions. So, the experimental validity of MIMO diversity performance is important to better understand robustness and real-world operational behaviour under the mismatch conditions at the ports of MIMO antenna or system.

In such a MIMO antenna system, diversity characteristics—such as the ECC, DG, TARC, and MEG—depend heavily on how independently the antenna elements operate. Introducing short and open loads (intentional or due to faults/mismatches) significantly alters these characteristics. The degree of correlation between the communication channels of the MIMO antenna is known as the envelope correlation coefficient (ECC) [7]. The ECC is expressed in terms of the radiation field patterns of the two-port diversity system as given in equation (1) [8]. Here, E^* is a complex conjugate of the electric field (E) pattern of the MIMO antenna for the θ and ϕ directions, and XPR is the cross-polarization ratio, which is the ratio of power in the co-polarized field to the cross-polarized field. The P_θ and P_ϕ are the angular power density in θ and ϕ directions, respectively. Although the ideal ECC value for a fully uncorrelated MIMO antenna is zero, an acceptable diversity performance requires a value between 0 and 0.5.

$$ECC_{ij} = \frac{\left|\oiint\left[XPR.E_{\theta_i}E^*_{\theta_j}P_\theta+E_{\phi_i}E^*_{\phi_j}P_\phi\right]d\Omega\right|^2}{\{\oiint\left[XPR.E_{\theta_i}E^*_{\theta_i}P_\theta+E_{\phi_i}E^*_{\phi_i}P_\phi\right]\mathrm{d}\Omega\times \oiint\left[XPR.E_{\theta_j}E^*_{\theta_j}P_\theta+E_{\phi_j}E^*_{\phi_j}P_\phi\right]d\Omega\}} \tag{1}$$

In terms of S-parameters, ECC can be obtained using equation (2) for the 2-port MIMO antenna:

$$\rho_e = \frac{|S^*_{11}S_{12}+S^*_{21}S_{22}|^2}{(1-|S_{11}|^2-|S_{21}|^2)(1-|S_{22}|^2-|S_{12}|^2)} \qquad ((2)$$

When any port is either open ($S_{ii} \rightarrow 1$) (high reflection) or short ($S_{ii} \rightarrow -1$), numerator correlation terms increase and reduce denominator efficiency, which leads to higher ECC.

The Diversity Gain (DG) of the MIMO system is the next essential parameter to evaluate its diversity performance. Equation (3) provides an expression to find DG using ECC [8].

$$DG_{ij} = 10\sqrt{1-\left(ECC_{ij}\right)^2} \tag{3}$$

With open or short loads at any port, DG drops as ECC increases. So the significant degradation in the MIMO performance is due to high correlation and reduced independent signal paths.

When operating multiple AEs simultaneously, the closely spaced AEs affect the system's performance, including gain, bandwidth, and efficiency. For this reason, the Total Active Reflection Coefficient (TARC) is a crucial metric for assessing the diversity performance of a MIMO antenna. To calculate TARC, the square root of the ratio of total reflected power to total incident power is taken as shown in equation (4). For an N×N MIMO antenna, TARC is defined as:

$$\text{TARC} = \sqrt{\frac{\sum_{i=1}^{N} \left|\sum_{k=1}^{N} S_{ik} e^{j\theta_k}\right|^2}{N}} \tag{4}$$

Where, N is the antenna ports, S_{ik}= S-parameters having i and k as the receiving port and transmitting port, respectively, and θ_k= phase of the excitation signal at port k.

The four-port MIMO/Diversity system's S-parameters can be used to produce TARC using equation (5), where θ_i presents the phase of the associated transmission (S_{mn}) parameter, i=1, 2, 3 [9] and ranges from 0 to 2π, m, n= 1, 2, 3, 4 for the four-port antenna. The TARC is preferred to be less than -10 dB for the perfect MIMO system. The open load at any port leads to a moderate increase in TARC due to full reflection but weaker coupling, while the short load leads to a severe increase in TARC due to strong coupling and phase inversion. As a result, both kinds of load degrade MIMO performance.

$$TARC = \sqrt{\frac{\sum_{i=1}^{4} \left|\sum_{k=1}^{4} S_{ik} e^{j\theta_k}\right|^2}{4}} \tag{5}$$

By utilizing the following equation (6) [8], the Mean Effective Gain (MEG) of the designed spatial diversity MIMO antenna for each port (Port 1, Port 2, Port 3, and Port 4) can be calculated. The MEG ratio (MEG_i/MEG_j) should be within ±3 dB for optimal diversity [10], i, j, k = 1, 2, 3, 4.

$$MEG_k = 0.5\left[1-|S_{k1}|^2-|S_{k2}|^2-|S_{k3}|^2-|S_{k4}|^2\right] \tag{6}$$

MEG becomes imbalanced when the MIMO antenna is terminated open or short at any port, resulting in the active element dominating and the open element contributing negligibly.

Thus, the efficiency of the MIMO system is reduced by power loss due to dissipation in short circuits and re-radiation with phase distortion. Another effect is the resonance shift as the shorted antenna element acts as a reactive load, which detunes the system. In this paper, an experimental study is conducted on diversity parameters, which are calculated from measured S-parameters. These S-parameters are obtained for a 4-port multiband MIMO antenna with matched, open, and short loads. Analysis of changes in diversity parameters is presented for the reliability of such an MIMO system.

2. Detail of the multiband MIMO antenna:

Fig. 1(a) depicts the proposed antenna's design, consisting of four antenna elements (AEs) operating at the four different 5G bands for the lower and mid-frequency ranges. The blue color shows the Cu layer, while the green color represents the etched area of the antenna schematic. A single-sided FR-4 substrate (ε_r = 4.3, tanδ = 0.02) measuring 150 × 120 × 1.5 mm³ is used to design the proposed antenna. The other dimensions (in mm) of this antenna are R=54, R2=44, F1=4, F2=3.8, F3=1.5, F4=1.2, G1=1, G2=1, G3=0.3, G4=0.5, G5=0.4, G6=0.6, W1=3.9, L1=3.9, W2=4.5, L2=18.2, W3=6.06, L3=10, W4=4.5, L4=10, W5=2, L5=5, and W6=9.7. It was fabricated and coated with a protective green layer, as shown in Fig. 1(b). The four antenna elements (AEs) are positioned at their four edges on the substrate's front side. AE1 is designed to cover the lower 5G band (<1 GHz), and the other three AEs, AE2, AE3, and AE4, cover different mid-frequency bands up to 6 GHz. To achieve high isolation between AE1 and AE2, a meander-line decoupling structure (DS) is integrated into the ground on the right side of AE1.

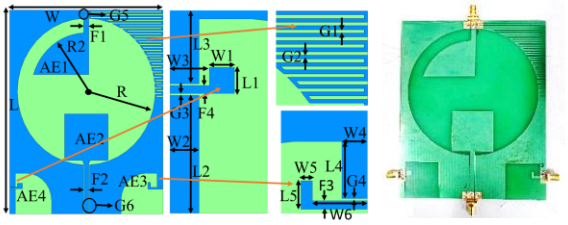

(a) (b)

Figure 1: Multi-band antenna (a) Schematic, (b) Actual photograph

In Fig. 1(a), AE1 offers a bandwidth of 0.55-0.89 GHz, AE2 offers a bandwidth of 1.27-2.82 GHz, AE3 provides an additional band of 3.05-4.34 GHz, and AE4 provides a final band of 4.47-6 GHz. Isolation between the AEs is shown in Fig. 1(b) when AE1 is excited. The isolation between AE1 and AE2 was>10 dB and >20 dB from AE3 and AE4, respectively, across the entire band up to 6 GHz.

The simulated responses of four AEs are shown in Fig. 2(a)-(d), which were obtained using the CST Microwave Studio software. The return loss levels well below -10 dB at the four intended bands (0.72-0.98 GHz, 1.62-2.66 GHz, 3.04-4.42 GHz, and 4.47-6 GHz). The inter-element isolation parameters show that the AEs exhibit high isolation performance, exceeding 15.01 dB throughout the four bands. Gains of 1.44 to 3.8 dB, 1.728 to 5.065 dB, 1 to 3.066 dB, and 2.75 to 4.61 dB are offered by the AE1, AE2, AE3, and AE4, respectively. The efficiency of AE1, AE2, AE3, and AE4 is 61.67-72.99%, 72.37-85.64%, 55.89-64.98%, and 67.93-80.07%, respectively.

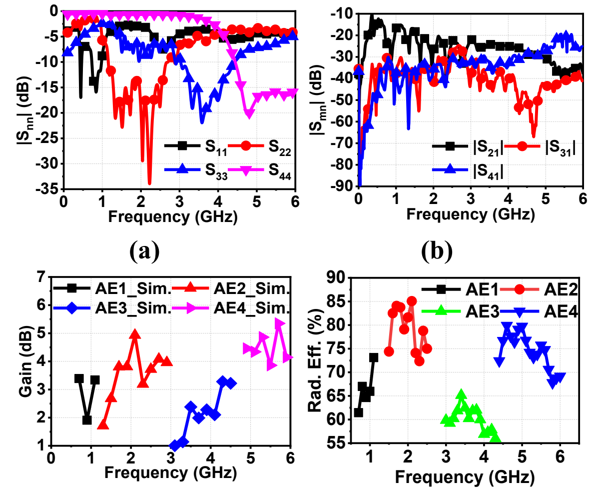

(a) (b)

(c) (d)

Figure 2: Simulation response of multi-band antenna (a) Reflection coefficient (S_{nn}), (b) Isolation (S_{mn}), (c) Gain, and (d) Efficiency.

Fig. 2 (c) displays the simulated gains of 1.44 to 3.8 dB, 1.728 to 5.065 dB, 1 to 3.066 dB, and 2.75 to 4.61 dB offered by the AE1, AE2, AE3, and AE4, respectively, at the four frequency bands over their corresponding operating ranges. Fig. 2(d) displays the simulated efficiencies of the AE1, AE2, AE3, and AE4, which are 61.67-72.99%, 72.37-85.64%, 55.89-64.98%, and 67.93-80.07%, respectively at the four respective operating bands.

2. Antenna Measurements with Different Loads:

The characteristics of the multiband antenna are measured with different loads upto 6 GHz using the Transcom T6 Vector network analyser (VNA). The setup is shown in Fig. 3, and S-parameters are measured by placing different types of loads on the multiband antenna's open ports after calibration. For measuring the S_{11} reflection parameter, the VNA's port 1 is connected to port 1 of the multiband antenna, while ports 2-4 of the multiband antenna are connected to matched loads. Then, S_{11} is measured by replacing matched loads with short terminations, and the final S_{11} readings are obtained with open terminations on ports 2 to 4 of the multiband antenna. These measured S_{11} parameters are compared with the simulated S_{11} in Fig. 4(a). Similarly, other transmission S-parameters (S_{21}, S_{31}, and S_{41}) are measured with different loads and presented in Fig. 4(b-d).

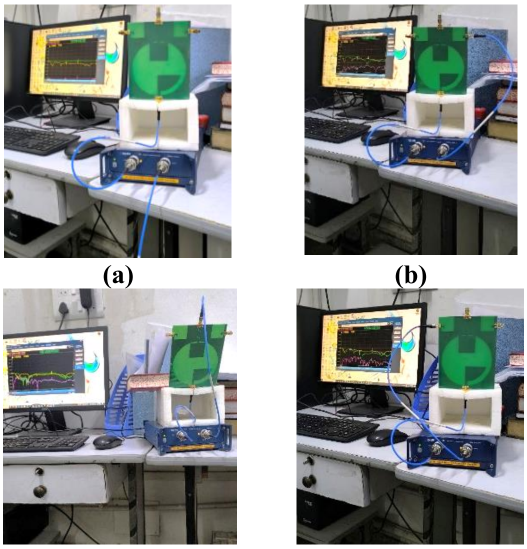
(a) (b)
(c) (d)

Figure 3: VNA setup of multi-band antenna (a) S_{11} measurement, (b) S_{21} measurement, (c) S_{31} measurement, and (d) S_{41} measurement.

3.1 Effect of different loads on S-parameters of multiband antenna:

The S-parameter responses, such as S_{11}, S_{21}, S_{31}, and S_{41}, of the multiband antenna with different loads are plotted in Figure 4. No significant differences in the S-parameters with different loads are observed compared to the simulated responses. This confirms that the effects on S-parameters are negligible due to different loads, since all ports operate over different frequency ranges. Also, the proposed antenna provides stable impedance matching, high isolation irrespective of whether the inactive ports are terminated with matched loads, open circuits or short circuits. This shows the robustness of the proposed antenna design for practical MIMO wireless communication applications. The small discrepancies between simulated and measured results are mainly due to fabrication tolerances, SMA connector soldering imperfections, and measurement uncertainties during VNA characterization. Additionally, the slight differences are caused due to differences in the dielectric constant, surface roughness and thickness of the FR-4 board. Regardless, the measured results have a good correspondence with the simulated data; hence, the effectiveness of the designed multiband MIMO antenna is proven.

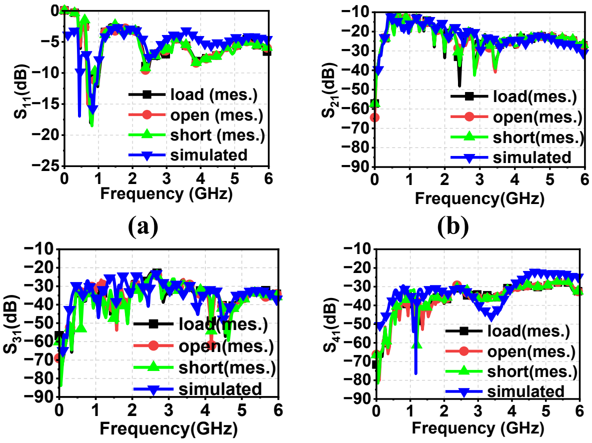

(a) (b)
(c) (d)

Figure 4: S-parameter responses of multiband antenna with different loads (a) S_{11} response, (b) S_{21} response, (c) S_{31} response, and (d) S_{41} response.

3.2 Effect of Different on Diversity Parameters of Multiband Antennas:

This section examines the various diversity parameters of the utilized multiband MIMO antenna, which are obtained from the measured S-parameters. Fig. 5(a) displays that the ECC values between ports 1-2, 1-3, and 1-4 are below 0.311, 0.314, and 0.302 in the operating bands for matched, open, and short load, respectively. The ECC values of ~0.3 (in <50 MHz bandwidth) indicate moderate correlation between AE1 and AE2 due to nearby operating bands. For other two AEs, ECC values are well below 0.02. So, the proposed antenna can still support diversity operation, even if the correlation level may slightly reduce channel capacity and DG compared to highly decoupled MIMO systems. The DG is approximately 10 dB, as shown in Fig. 5(b). Additionally, the plots show that the presented MIMO antenna provides good spatial diversity across the operating bandwidth, with similar high DG and low ECC for all three loads.

Fig. 5(c) plots the TARC results as a function of frequency for the three cases (Case 1=$\theta_1 = 0^{\circ}, \theta_2 = 90^{\circ}, \theta_3 = 180^{\circ}$; Case2=$\theta_1 = 0^{\circ}, \theta_2 = 90^{\circ}, \theta_3 = 270^{\circ}$; Case3=$\theta_1 = 0^{\circ}, \theta_2 = 180^{\circ}, \theta_3 = 90^{\circ}$) using equation (5). The minimum TARC values of -8.272 dB, -8.223 dB, and -8.035 dB over the relevant bandwidth are calculated for these cases, which are slightly higher than -10 dB. The reported TARC values (~ -8 dB) are above the commonly accepted threshold of -10 dB for good MIMO performance. This shows that a large portion of incident power is reflected back, which reduces the overall efficiency and degrades the multiplexing capability of the antenna. Although the obtained TARC values still demonstrate acceptable multiport operation, the performance may not be optimal for high-efficiency MIMO applications. Also, the TARC values lie within the same range obtained with matched, open, and short loads, respectively.

The MEG$_k$ results for k=1, 2, 3, and 4 for Port= 1, 2, 3, and 4 are presented in Fig. 5(d), along with the MEG ratios between the dual ports. The MEG ratios are within ±3 dB across 4-6 GHz. Similar to the TARC values, negligible differences have been observed in the MEG values when connecting the matched, open, and short loads.

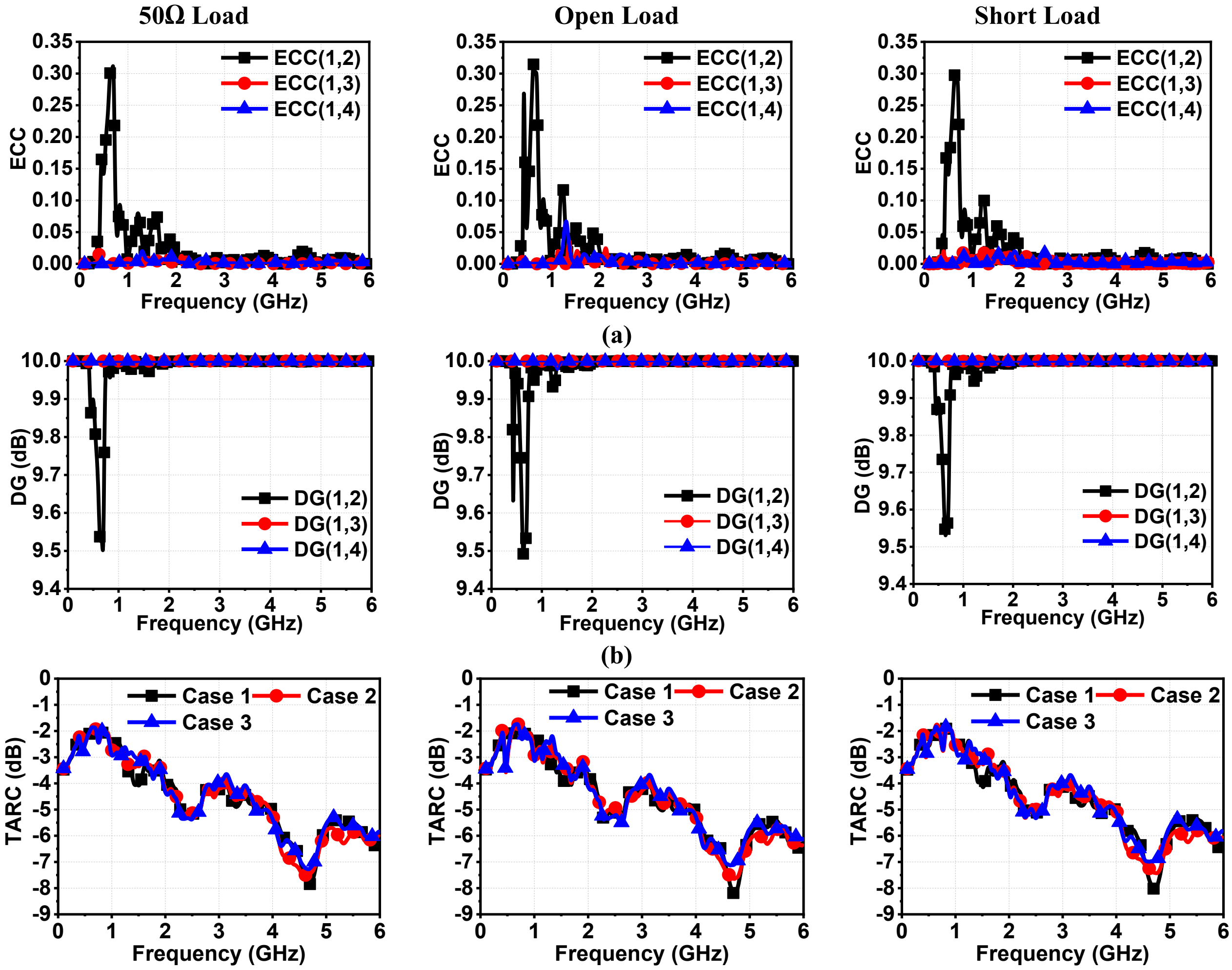

(a)

(b)

(c)

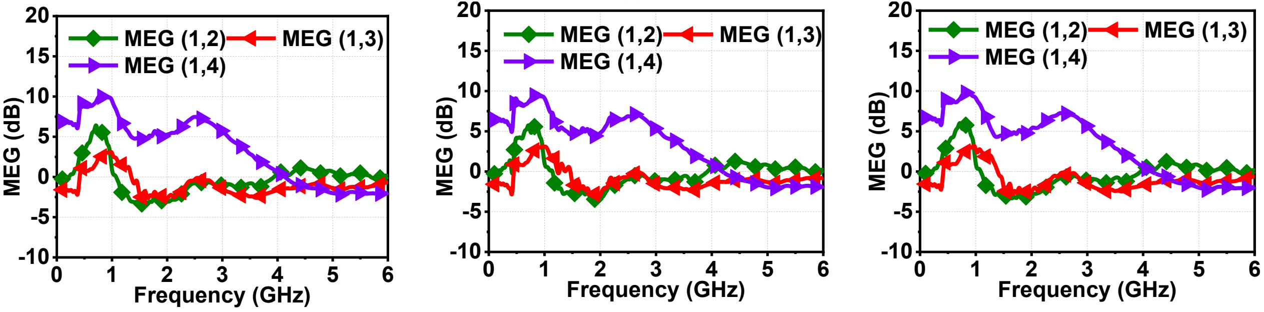

(d)

Figure 5: Diversity response of multi-band antenna under different loads (a) ECC, (b) DG, (c) TARC, and (d) MEG.

3. Conclusions:

In this work, the effect of different loads on the diversity parameters of the multiband MIMO antenna is investigated. The open and short loads increase reflection at the respective antenna ports and affect the reflection and transmission in a multiport system. Thus, both degrade the current distribution, transmission independence, and channel orthogonality in MIMO systems; hence, proper termination is critical for maintaining low ECC and high diversity gain. In the case of the multiband antenna, where each antenna element operates in a different frequency band, the variation in loads at the unused ports has no significant effect on diversity parameters.

Acknowledgements:

Authors are thankful to the Faculty Research Programme (FRP) of the Institute of Eminence (IoE), University of Delhi (Letter Ref. /No./IoE/2025-26/12/FRP dated 30.10.2025) for financial support.

Conflict of Interest:

Authors declare no conflicts of interest.

References:

[1] Puneet Sehgal, Kamlesh Patel, "Triband Dual Port h-SRR MIMO Antenna for WLAN/WiMAX/Wi-Fi 6 Applications," *Progress In Electromagnetics Research M,* vol. 123, pp. 35-43, 2024.

[2] Shailesh, G. Srivastava, S. Kumar, S. Ibrahim Alshathri, W. El-Shafai and O. Prakash Kumar, "Compact UWB MIMO Antenna With a Modified Back Reflector and Supported by Characteristic Mode Analysis for Wireless Communication Applications," *IEEE Access,* vol. 12, pp. 187302-187312, 2024.

[3] Shailesh, G. Srivastava, M. Al-Hamami, S. Kumar, S. M. P and O. P. Kumar, "Triple-Band Notched and Highly Decoupled MIMO Antenna Using Characteristic Mode Analysis," *IEEE Access,* vol. 13, pp. 165956-165969, 2025.

[4] Shailesh, S,M. Patel, and K. Patel, "Performance of 4 × 4 ring decoupling structure-based UWB MIMO antennas for transceiver applications in

simultaneous transmit and receive configuration," *Optical and Quantum Electronics,* vol. 58, p. 271, 2026.

[5] A. Srivastava et al., "Performance of two-element meander line MIMO antenna for Wi-Fi Internet of Things applications," *Journal of Electromagnetic Waves and Applications,* vol. 39, no. 14, pp. 1718-1734, 2025.

[6] M. K. Khan, S. Liu, and M. I. Khan, "A Wideband Eight-Port MIMO Antenna with Reduced Mutual Coupling for Future 5G mm-Wave Applications," *Sensors,* vol. 25, no. 2, p. 484, 2025.

[7] A. Kumar, A. Q. Ansari, B.K. Kanaujia, J. Kishor, and S. Kumar, "An Ultra-Compact Two-Port UWB-MIMO Antenna with Dual Band-Notched Characteristics," *AEU-International Journal of Electronics and Communications,* vol. 114, p. 152997, 2020.

[8] A. K. Chaudhary and M. Manohar, "A Modified SWB Hexagonal Fractal Spatial Diversity Antenna With High Isolation Using Meander Line Approach," *IEEE Access,* vol. 10, pp. 10238-10250, 2022.

[9] C. Yu et al., "A Super-Wideband and High Isolation MIMO Antenna System Using a Windmill-Shaped Decoupling Structure," *IEEE Access,* vol. 8, pp. 115767-115777, 2020.

[10] Sasmita Pahadsingh, Sudhakar Sahu, "Four port MIMO integrated antenna system with DRA for cognitive radio Platforms," *AEU - International Journal of Electronics and Communications,* vol. 92, pp. 98-110, 2018.

Current Natural Sciences & Engineering
Volume 3, Issue 1, 2026, 954-963

Design and Characterization of 2D $Ti_3C_2T_x$ MXene as an Efficient Electrode Material for Supercapacitor

Mahaveer Singh[1], Bheem Kumar[1], Pushpendra Kumar Meena[1] and Kedar Singh[1]*

[1]School of Physical Sciences, Jawaharlal Nehru University (JNU), New Delhi 110067, India

Received date:08/05/206, Acceptance date: 12/06/2026

***DOI:* http://doi.org/10.63015/8ms-2500.3.1**

**Corresponding Author:* kedar@mail.jnu.ac.in

Abstract

The increasing demand for effective energy storage devices has enhanced the need of durable electrode materials for supercapacitors. In this work, $Ti_3C_2T_x$ MXene nanosheets was synthesized via HF etching and subsequent delamination to obtain layered 2D nanosheets. The structural and morphological properties were examined using XRD pattern, SEM, and TEM, confirming the successful synthesis of layered structure, while UV–Visible spectroscopy indicated its optical response. The electrochemical performance was evaluated in a three-electrode setup using nickel foil as the current collector substrate. Cyclic voltammetry (CV) and galvanostatic charge–discharge (GCD) measurements show excellent capacitive behaviour, delivering a notable specific capacitance of 535 F g^{-1} at current density of 1 A g^{-1}. Electrochemical impedance spectroscopy (EIS) revealed low R_s and efficient charge transfer kinetics, supporting enhanced electrochemical performance. The superior capacitance is due to the high conductivity, wide surface area, and rapid ion transport within the $Ti_3C_2T_x$ MXene nanosheets, demonstrating that $Ti_3C_2T_x$ is an effective electrode material for high performing supercapacitor application.

Keywords: MXene; $Ti_3C_2T_x$; Supercapacitors; Electrochemical Studies; Energy Storage.

1. Introduction

In growing world, the use of green energy resources has accelerated the development of energy storage devices such as supercapacitor and batteries [1–3]. Supercapacitor are well recognized for high-power density, quick charge discharge capabilities, long term cyclic stability, cost effective, and environment friendly [4–8]. Flexible supercapacitor provides significant benefits over traditional supercapacitor, including lightweight, great flexibility, and compact size making them ideal for portable electronics [9]. Electrodes are critical for tuning the electrochemical performance of supercapacitor. Two-dimensional nanomaterials have gained popularity due to their increased surface area, high electronic conductivity, and mechanical compatibility[10]. As a promising material for supercapacitor application are 2D transition metal dichalcogenides (TMDs) and MXene have been explored due to high surface area and mechanical flexibility [11–15].

Among various electrochemical materials, a family of 2D transition metal carbide/nitrides are promising electrode material for energy storage for owing to their adaptable properties such as high electrical conductivity, electrochemical versatility, large surface area, easy to synthesis, easily accessible tunable morphology, and superficial electrolyte/ion transport through widely interlayered spacing [16–18]. MXene are often obtained from MAX phase, which are which are layered ternary ceramic materials given by the formula $M_{n+1}AX_n$ ($n = 1–4$), where M is a transition metal like Ti, V, Zr, Mo, Hf, Mo, Nb, etc., A is a group 13 or 14 element, and X is N and/or C. The prepared MXene are denoted as $M_{n+1}XnT_x$, where T_x stands for surface terminations such as F, O, OH, and Cl[19]. $Ti_3C_2T_x$ is the most extensively investigated MXene because of its high stability [20]. However, MXene have some drawbacks, including restacking inclination due to intense hydrogen bonding and weak van der wall interaction, superficial flaws in colloidal solution, and low flexibility, which have limited their current applications [21,22]. The main determinants of high electrochemical performance are the operative methodological characteristics, structural robustness, high electrically conductive, and abundance of active sites. Priyanka et al. achieved capacity of $Ti_3C_2T_x$ in 5 M KOH electrolyte is 368.5 F g^{-1} [23]. Xu et al. found the specific capacitance of $Ti_3C_2T_x$-rGO composite is 154 F g^{-1} at a current density of 2 A g^{-1} in electrolyte 6 M KOH [24].

In present work, $Ti_3C_2T_x$ MXene nanosheets were synthesized by HF-etching method, trailed by exfoliation in LiCl solutions to attain delaminated material. Structural (XRD) and Morphological (SEM and TEM) analysis gives the agreement for successful synthesis if $Ti_3C_3T_x$ sheets. Using a three-electrode setup, the electrochemical performance of pristine $Ti_3C_2T_x$ MXene nanosheets was methodically assessed. The charge-storage and resistance behavior of the electrode material evaluated using thorough electrochemical tests, like cyclic voltammetry (CV), galvanostatic charge–discharge (GCD), and electrochemical impedance spectroscopy (EIS). The active substance was fabricated on nickel foil to create the working electrodes, and 1 M H_2SO_4 electrolyte was used for all electrochemical tests. According to the GCD tests, the $Ti_3C_2T_x$ MXene electrode produced a huge specific capacity of 535 F g^{-1} at a current density of 1 A g^{-1}. Similarly, a specific capacity of 387.5 F g^{-1} was found by CV analysis at scan rate 20 mV s^{-1}. $Ti_3C_2T_x$ MXene nanosheets is distinctive two-dimensional layered design, which provides a huge accessible surface area, superior electronic conductivity, and an abundance of electro-chemical active sites for effective ion transport and charge transfer, is responsible for the improved electrochemical performance. These results shown for $Ti_3C_2T_x$ MXene is great promise as an electrode material for advanced energy storage device, especially high-performance supercapacitor.

2. Experimental Section

2.1. Materials

Ti_3AlC_2 MAX phase (99 %, Sigma Aldrich), HF (48 %, Thermo Fisher Scientific, India Pvt.) and HCl (37 %, Thermo Fisher Scientific), H_2SO_4 (98 %, Thermo Fisher Scientific), ethanol (CH_3CH_2OH) (99.7%, Sigma Aldrich), and deionized water (DI) used for preparing all of the solutions during synthesis process. All of the materials are of analytical grade and used without any purification.

2.2. Synthesis of MXene ($Ti_3C_2T_x$)

The $Ti_3C_2T_x$ MXene was synthesized using the Ti_3AlC_2 MAX phase by chemical etching using hydrofluoric acid (HF). First, 6 mL of deionized (DI) water, 12 mL HCl, and 2 mL of HF were combined in Teflon tube and agitated at 355 rpm. Subsequently, 1 g Ti_3AlC_2 MAX powder gently add to the etchant solution. The HF removed Al layer by generating AlF_3, resulting to the development of multilayer $Ti_3C_2T_x$. For 24 h, the mixture was constantly mixed. Following etching, the reaction mixture was centrifuged at 5000 rpm to repeatedly wash it with DI water till the pH obtain nearly neutral. The cleansed $Ti_3C_2T_x$ suspension was then mixed with 1 g of LiCl and agitated in a three-neck flask at 60 °C for two hours [25]. The delamination of MXene layers was made easier by this intercalation stage shown in **Fig. 1**. Following intercalation, the product was again purified by several centrifugation cycles at 5000 rpm to remove remaining salts and acids. Finally, the resulting $Ti_3C_2T_x$ MXene powder was dry in a vacuum oven at 80 °C for overnight.

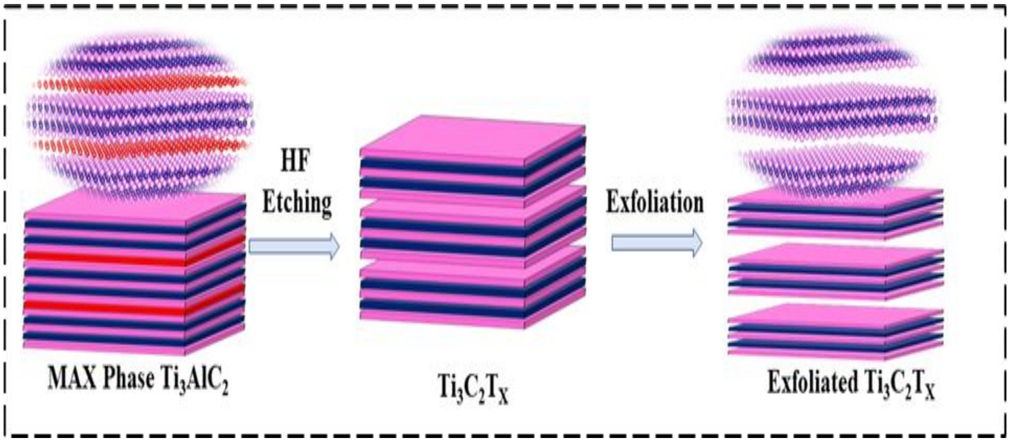

Figure 1. Graphic demonstration of synthesis of $Ti_3C_2T_x$ MXene nanosheets

2.3.Characterization

X-ray diffraction (XRD) measurement using Rigaku MiniFlex 600 diffraction were used to investigate crystallographic structure of the prepared material. Optical analysis is done by UV absorption spectra. Scanning electron microscopy (SEM; Zeiss EVO40) was used to examine the surfaces morphology of $Ti_3C_2T_x$ and by using TEM/HRTEM (JEOL 2100F, 200 kV), the morphology was thoroughly investigated, providing complete insights of interlayer spacing, morphological characteristics, and crystalline framework.

2.4. Electrochemical Measurements

The electrochemical measurements of $Ti_3C_2T_x$ MXene nanosheets was performed using Metrohm Autolab potentiostat/galvanostat (PGSTAT204) in a three-electrode setup in 1 M H_2SO_4 electrolyte. The working electrodes were the synthesized nanomaterials, and the reference and counter electrodes are Ag/AgCl and Platinum wire, respectively. The working electrode were fabricated by coating slurry having 80% $Ti_3C_2T_x$ MXene, 10% carbon black, and 10% PVDF as binder in NMP onto the nickel foam substrate and was dry for 12 hrs at 70 °C in vacuum oven. Charge storage behavior, rate capability, and interfacial kinetics were studied by cyclic voltammetry (CV), galvanostatic charge-discharge (GCD), and electrochemical impedance spectroscopy (EIS). GCD tests was performed for 1-3 A g^{-1} current densities within the potential window established by CV analysis, and CV was conducted scan rate of 20-100 mV s^{-1}. The identical electrochemical setup was used to record EIS spectra throughout a frequency range of 0.01-10^5 Hz.

3. Result and Discussion

3.1. Structural and UV-Visible absorption analysis

The crystal structure of $Ti_3C_2T_x$ MXene nanosheets was investigated by X-ray diffraction (XRD) demonstrated in **Fig. 2(a)**. The spectra of $Ti_3C_2T_x$ MXene sheets having a strong peak at angle 6.97°, 14.95°, 27.66°, 35.03°, 41.21°, 57.75° and 61.11° corresponding to the planes (002), (004), (006), (101), (105), (109) and (110), which confirms the successfully synthesis of $Ti_3C_2T_x$ MXene [26]. The removal of Al using HF acid etching process results in wide interplanar spacing, the d-spacing corresponding to the plane (002) is 1.16 nm. The crystallite size of $Ti_3C_2T_x$ MXene was found to be 13.21 nm, observed by Debye-Scherrer formula.

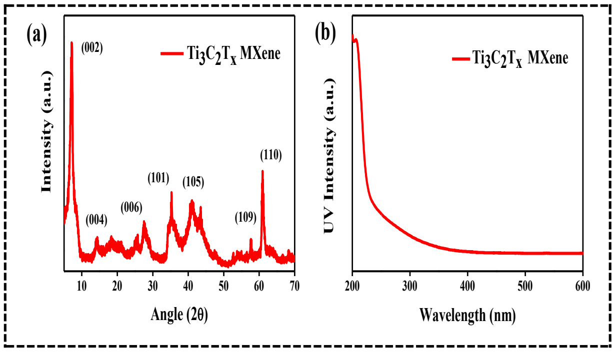

Figure. 2. (a) XRD pattern, (b) UV absorption spectra of $Ti_3C_2T_x$ MXene.

The optical properties were investigated by analyzing the UV absorption spectra of $Ti_3C_2T_x$ MXene nanosheets. As seen in **Fig. 2(b)**, the $Ti_3C_2T_x$ MXene nanosheets absorbance borders extend into the visible spectrum, with maximal absorbance points of around 208 nm. Furthermore, the Tauc plot has been used to measure the optical bandgap power of $Ti_3C_2T_x$ MXene nanosheets, which have intrinsic linear bandgaps of 1.24 eV [27].

3.2. Scanning electron microscopic (SEM) and Transmission electron microscopic (TEM) analysis

The SEM image of $Ti_3C_2T_x$ MXene nanosheets is demonstrated in **Fig. 3(a)**, which offers important morphological insights and reveals their distinctive layered shape. The residual van der Waals interactions between neighboring $Ti_3C_2T_x$ layers are responsible for the observed stacked sheet-like architecture. The TEM image of $Ti_3C_2T_x$ MXene at a scale of 100 nm is presented in

Fig. 3(b), which further supports the material's ultrathin sheet-like shape. Additionally, the HR-TEM image of $Ti_3C_2T_x$ MXene at resolution (5 nm) is shown in **Fig. 3(c)**. It clearly shows discrete lattice fringes having interlayer spacing of 1.12 nm, which is indicative of the well-defined crystalline structure [25,28].

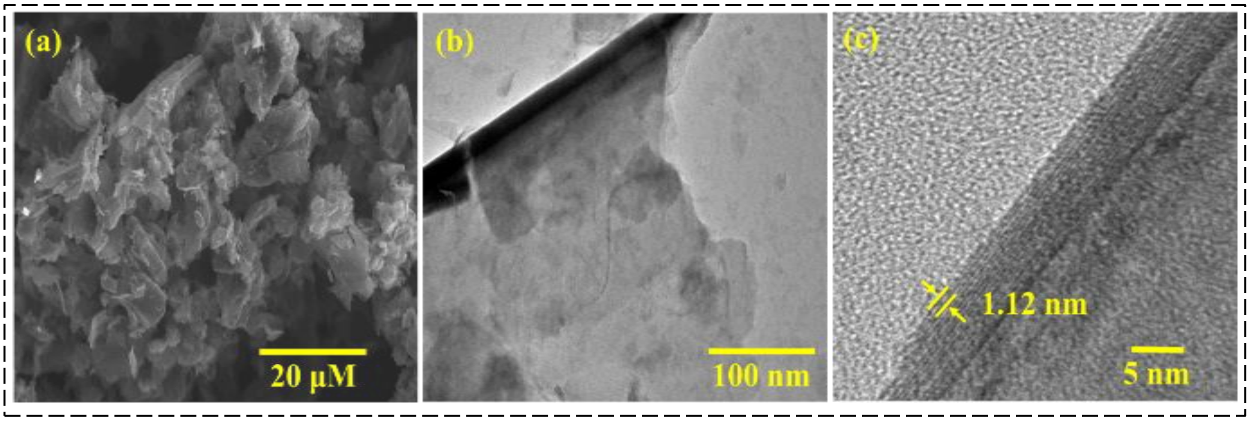

Figure 3. (a) SEM image of $Ti_3C_2T_x$ MXene, (b) TEM image of $Ti_3C_2T_x$ MXene nanosheets, (c) HR-TEM image of $Ti_3C_2T_x$ MXene nanosheets.

Electrochemical Measurements

Cyclic voltammetry (CV) and Galvanostatic charge-discharge (GCD) was used to systematically measure the electrochemical measurement of $Ti_3C_2T_x$ MXene. $Ti_3C_2T_x$ MXene nanosheets were used as the working substance, Pt wire as counter electrode, and Ag/AgCl electrode as reference electrode in a three-electrode setup for electrochemical measurements. Every measurement was performed in a potential range of -0.12 to -0.32 V in a 1 M H_2SO_4 acidic electrolyte. The following formula was used to determine the electrode's specific capacitance (C_{sp}): m is the mass of the working substance coated on nickel foam; k is scanning speed varying from (20–100 mV s^{-1}); ΔV is the potential span of (0.2 V); and ∫ Idv is the integrated area under the CV curve[29].

$$C_s = \frac{\int \mathrm{Idv}}{mk\Delta V} \tag{1}$$

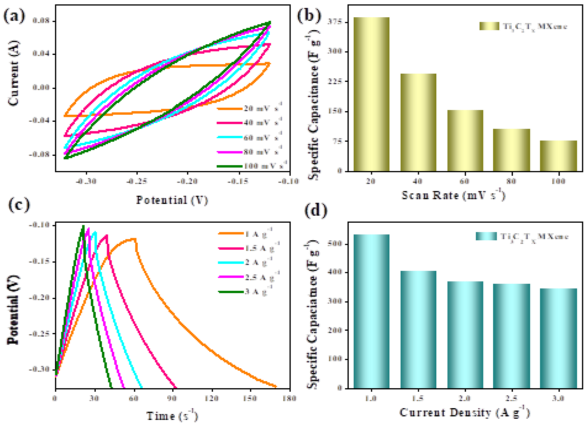

Figure 4. (a) CV measurements of Ti3C2Tx MXene, (b) Comparison bar chart of the CV

The CV profile of $Ti_3C_2T_x$ MXene nanosheets is presented in **Fig. 4(a)**, and computed specific capacitance values for $Ti_3C_2T_x$ MXene nanosheets were 387.5, 244.24, 155.32, 105.74, and 77 F g^{-1}, at scan rate 20, 40, 60, 80, and 100 mV s^{-1}. Because

Table 1: Comparison of the electrochemical behaviour of $Ti_3C_2T_x$ MXene based Supercapacitor.

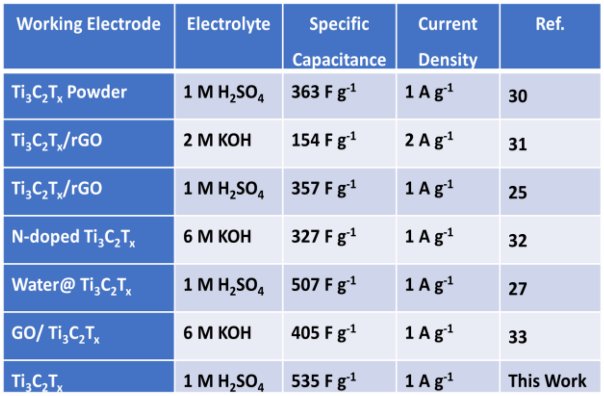

Working Electrode	Electrolyte	Specific Capacitance	Current Density	Ref.
$Ti_3C_2T_x$ Powder	1 M H_2SO_4	363 F g^{-1}	1 A g^{-1}	30
$Ti_3C_2T_x$/rGO	2 M KOH	154 F g^{-1}	2 A g^{-1}	31
$Ti_3C_2T_x$/rGO	1 M H_2SO_4	357 F g^{-1}	1 A g^{-1}	25
N-doped $Ti_3C_2T_x$	6 M KOH	327 F g^{-1}	1 A g^{-1}	32
Water@ $Ti_3C_2T_x$	1 M H_2SO_4	507 F g^{-1}	1 A g^{-1}	27
GO/ $Ti_3C_2T_x$	6 M KOH	405 F g^{-1}	1 A g^{-1}	33
$Ti_3C_2T_x$	1 M H_2SO_4	535 F g^{-1}	1 A g^{-1}	This Work

of restricted ion diffusion and decreased electrolyte accessibility at high scan rates, specific capacity gradually decreases as scan rate increases. The $Ti_3C_2T_x$ MXene electrode's specific capacitance as a function of scan rate is demonstrated in **Fig. 4(b)** Additionally, the specific capacity of the $Ti_3C_2T_x$ MXene electrode was assessed using galvanostatic charge-discharge (GCD) experiments at numerous current densities between 1 and 3 A g^{-1} within the potential span of −0.12 to −0.32 V (vs. Ag/AgCl electrode). The GCD profiles of the $Ti_3C_2T_x$ MXene electrode recorded at various current densities are seen in **Fig. 4(c)**. These profiles show almost symmetric charge-discharge curves, which are suggestive of good capacitive performance and electrochemical reversibility [27].

$$C_s = \frac{I_m \Delta t}{\Delta V} \qquad (2)$$

The above formula was used to get the specific capacity (C_{sp}) of the three-electrode system: C_{sp} is the specific capacity, I_m is applied current density, Δt is discharging time, and ΔV is the potential span. The computed specific capacity of $Ti_3C_2T_x$ MXene were 535, 405, 370, 362.5, and 345 F g^{-1} at current densities of 1, 1.5, 2, 2.5, and 3 A g^{-1} respectively. The fast speed of ions at higher current density is the reason for the decrease in specific capacitance. The $Ti_3C_2T_x$ MXene electrode's rate capability is demonstrated in **Fig. 4(d)**, which demonstrates the specific capacity as a function of current density. The Comparison of the electrochemical behavior of $Ti_3C_2T_x$ MXene based electrode materials for supercapacitor have shown in **Table 1.**

In 1 M H_2SO_4 electrolyte, $Ti_3C_2T_x$ sheets exhibits capacitive charge storage governed by fast, reversible H^+ intercalation/deintercalation within its interlayer corridors along with surface oxidation-reduction reactions of Ti positions. The plentiful –O, –OH, and –F functional groups facilitate strong interaction with H^+ ions, while the high electrical conductivity supports rapid electron movement. Additionally, the layered structure with engorged interlayer spacing encourages efficient ion diffusion and accessibility of active sites. This synergistic mechanism outcomes in high capacitance and rate capability.

3.3. Electrochemical impedance spectroscopy (EIS)

The impedance characteristics and charge storage behavior of $Ti_3C_2T_x$ MXene nanosheets were examined using electrochemical impedance spectroscopy (EIS) throughout a frequency span of 0.01 Hz to 10^5 Hz. **Fig. 5** shows the $Ti_3C_2T_x$ MXene Nyquist plot (red curve). The EIS spectrum shows a roughly linear trend in the low-frequency values and a noticeable semicircular arc in the high-frequency values. The semicircle's shape and size offer important information on the ion transport kinetics and interfacial electrochemical reactions taking place at the electrode–electrolyte interface, while its diameter correlates to charge-transfer resistance (R_{ct}) [28].

The electrochemical properties of the system are further clarified by the fitted curve (black curve in Fig. 5). The intrinsic resistance of the electrolyte, represented by the solution resistance (R_s), was found to be 0.83 Ω. In the meantime, it was determined that the electrode–electrolyte interface's charge-transfer resistance (R_{ct}) was 3.14 Ω, indicating effective charge transfer kinetics. Additionally, the $Ti_3C_2T_x$ MXene electrode's dominating capacitive nature and advantageous ion transport features are confirmed by the linear behavior shown in the low-frequency zone.

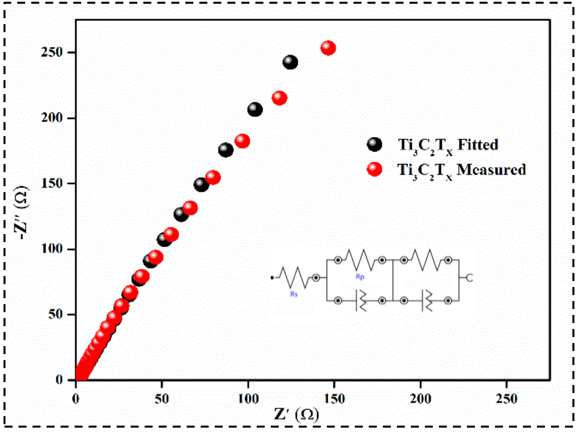

Figure. 5. Nyquist measured and fitted curves of $Ti_3C_2T_x$ MXene.

4. Conclusion

This study shows that, $Ti_3C_2T_x$ MXene nanosheets was successfully synthesized through HF etching and delamination, yielding a 2D layered structure. Structural and morphological analyses using XRD, SEM, and TEM validate the formation of few-layer $Ti_3C_2T_x$ MXene sheets with prolonged interlayer spacing, while UV–Visible spectroscopy confirmed its optical features. Electrochemical measurements in a 3-electrode setup on nickel foam demonstrated outstanding capacitive performance, attaining a large specific capacitance of 535 F g^{-1} at 1 A g^{-1}. The CV and GCD results revealed fast charge storage ability, while EIS analysis showed low R_{ct} (3.14 Ω) and efficient charge movement. The enhanced electrochemical behaviour is mainly attributed to the high electrical conductivity, available superficial area, and fast ion transport pathways within the $Ti_3C_2T_x$ MXene nanosheets. Overall, these findings reveal $Ti_3C_2T_x$ MXene as a highly promising material for electrode in revolutionary high-performance supercapacitors.

Acknowledgements

M. Singh expresses gratitude to CSIR, New Delhi, India for providing financial support in the shape of the CSIR-JRF fellowship. For financing support under project ANRF/PAIR/2025/000029/PAIR-A, we are deeply grateful to the Anusandhan National Research Foundation (ANRF), Department of Science and Technology (DST), Government of India. The authors further thank the Central Instrumentation Facility (CIF), School of Physical Sciences (SPS), Jawaharlal Nehru University (JNU), and the Advanced Instrumentation Research Facility (AIRF), JNU, for providing access to sophisticated characterization instruments.

References

(1) Zhu, Q.; Li, J.; Simon, P.; Xu, B. Two-Dimensional MXenes for Electrochemical Capacitor Applications: Progress, Challenges and Perspectives. *Energy Storage Materials* **2021**, *35*, 630–660. https://doi.org/10.1016/j.ensm.2020.11.035.

(2) Tian, Z.; Sun, Z.; Shao, Y.; Gao, L.; Huang, R.; Shao, Y.; Kaner, R. B.; Sun, J. Ultrafast Rechargeable Zn Micro-Batteries Endowing a Wearable Solar

Charging System with High Overall Efficiency. *Energy Environ. Sci.* **2021**, *14* (3), 1602–1611. https://doi.org/10.1039/D0EE03623D.

(3) Kim, H.-K.; Kamali, A. R.; Roh, K. C.; Kim, K.-B.; Fray, D. J. Dual Coexisting Interconnected Graphene Nanostructures for High Performance Supercapacitor Applications. *Energy Environ. Sci.* **2016**, *9* (7), 2249–2256. https://doi.org/10.1039/C6EE00815A.

(4) Rani, D.; Dubey, A.; Kumar, B.; Singh, M.; Sharma, A. L.; Hussain, A. M. P.; Singh, K.; Kumar, P. Hydration-Engineered Widely Interlayered Vanadium Oxide Nanobelts for High-Performance Aqueous Zinc-Ion Batteries. *Batteries & Supercaps* **2026**, *9* (5), e70300. https://doi.org/10.1002/batt.70300.

(5) Lang, X.; Hirata, A.; Fujita, T.; Chen, M. Nanoporous Metal/Oxide Hybrid Electrodes for Electrochemical Supercapacitors. *Nature Nanotech* **2011**, *6* (4), 232–236. https://doi.org/10.1038/nnano.2011.13.

(6) Sengottaiyan, C.; Kalam, N. A.; Jayavel, R.; Shrestha, R. G.; Subramani, T.; Sankar, S.; Hill, J. P.; Shrestha, L. K.; Ariga, K. BiVO4/RGO Hybrid Nanostructure for High Performance Electrochemical Supercapacitor. *Journal of Solid State Chemistry* **2019**, *269*, 409–418. https://doi.org/10.1016/j.jssc.2018.10.011.

(7) Kim, Y.; Park, T.; Na, J.; Yi, J. W.; Kim, J.; Kim, M.; Bando, Y.; Yamauchi, Y.; Lin, J. Layered Transition Metal Dichalcogenide/Carbon Nanocomposites for Electrochemical Energy Storage and Conversion Applications. *Nanoscale* **2020**, *12* (16), 8608–8625. https://doi.org/10.1039/D0NR01664K.

(8) Simon, P.; Gogotsi, Y.; Dunn, B. Where Do Batteries End and Supercapacitors Begin? *Science* **2014**, *343* (6176), 1210–1211. https://doi.org/10.1126/science.1249625.

(9) Yang, P.; Mai, W. Flexible Solid-State Electrochemical Supercapacitors. *Nano Energy* **2014**, *8*, 274–290. https://doi.org/10.1016/j.nanoen.2014.05.022.

(10) Kumar, P.; Srivastava, P.; Singh, J.; Belwal, R.; Pandey, M. K.; Hui, K. S.; Hui, K. N.; Singh, K. Morphological Evolution and Structural Characterization of Bismuth Telluride (Bi_2 Te_3) Nanostructures. *J. Phys. D: Appl. Phys.* **2013**, *46* (28), 285301. https://doi.org/10.1088/0022-3727/46/28/285301.

(11) Pumera, M. Graphene-Based Nanomaterials and Their Electrochemistry. *Chem. Soc. Rev.* **2010**, *39* (11), 4146. https://doi.org/10.1039/c002690p.

(12) Liu, C.; Yu, Z.; Neff, D.; Zhamu, A.; Jang, B. Z. Graphene-Based Supercapacitor with an Ultrahigh Energy Density. *Nano Lett.* **2010**, *10* (12), 4863–4868. https://doi.org/10.1021/nl102661q.

(13) Mansourpanah, Y. MXenes and Other 2D Nanosheets for Modification of Polyamide Thin Film Nanocomposite Membranes for Desalination. *Separation and Purification Technology* **2022**, *289*, 120777. https://doi.org/10.1016/j.seppur.2022.120777.

(14) Kim, S.; Wang, H.; Lee, Y. M. 2D Nanosheets and Their Composite Membranes for Water, Gas, and Ion Separation. *Angewandte Chemie* **2019**, *131* (49), 17674–17689. https://doi.org/10.1002/ange.201814349.

(15) Prasad, J.; Singh, A. K.; Tomar, M.; Gupta, V.; Singh, K. Hydrothermal Synthesis of Micro-Flower like Morphology Aluminum-Doped MoS2/rGO Nanohybrids for High Efficient Electromagnetic Wave Shielding Materials. *Ceramics International* **2021**, *47* (11), 15648–15660. https://doi.org/10.1016/j.ceramint.2021.02.135.

(16) Lukatskaya, M. R.; Kota, S.; Lin, Z.; Zhao, M.-Q.; Shpigel, N.; Levi, M. D.; Halim, J.; Taberna, P.-L.; Barsoum, M. W.; Simon, P.; Gogotsi, Y. Ultra-High-Rate Pseudocapacitive Energy Storage in Two-Dimensional Transition Metal Carbides. *Nat Energy* **2017**, *2* (8), 17105. https://doi.org/10.1038/nenergy.2017.105.

(17) Anasori, B.; Lukatskaya, M. R.; Gogotsi, Y. 2D Metal Carbides and Nitrides (MXenes) for Energy Storage. *Nat Rev Mater* **2017**, *2* (2), 16098. https://doi.org/10.1038/natrevmats.2016.98.

(18) Hussain, S.; Vikraman, D.; Ali Sheikh, Z.; Taqi Mehran, M.; Shahzad, F.; Mujasam Batoo, K.; Kim, H.-S.; Kim, D.-K.; Ali, M.; Jung, J. WS2-Embedded MXene/GO Hybrid Nanosheets as Electrodes for Asymmetric Supercapacitors and Hydrogen Evolution Reactions. *Chemical Engineering Journal* **2023**, *452*, 139523. https://doi.org/10.1016/j.cej.2022.139523.

(19) Shekhirev, M.; Shuck, C. E.; Sarycheva, A.; Gogotsi, Y. Characterization of MXenes at Every Step, from Their Precursors to Single Flakes and Assembled Films. *Progress in Materials Science* **2021**, *120*, 100757. https://doi.org/10.1016/j.pmatsci.2020.100757.

(20) VahidMohammadi, A.; Mojtabavi, M.; Caffrey, N. M.; Wanunu, M.; Beidaghi, M. Assembling 2D MXenes into Highly Stable Pseudocapacitive Electrodes with High Power and Energy Densities. *Advanced Materials* **2019**, *31* (8), 1806931. https://doi.org/10.1002/adma.201806931.

(21) Kshetri, T.; Tran, D. T.; Le, H. T.; Nguyen, D. C.; Hoa, H. V.; Kim, N. H.; Lee, J. H. Recent Advances in MXene-Based Nanocomposites for Electrochemical Energy Storage Applications. *Progress in Materials Science* **2021**, *117*, 100733. https://doi.org/10.1016/j.pmatsci.2020.100733.

(22) Xu, X.; Yang, L.; Zheng, W.; Zhang, H.; Wu, F.; Tian, Z.; Zhang, P.; Sun, Z. MXenes with Applications in Supercapacitors and Secondary Batteries: A Comprehensive Review. *Materials Reports: Energy* **2022**, *2* (1), 100080. https://doi.org/10.1016/j.matre.2022.100080.

(23) Priyanka; Rundla, A.; Singh, M.; Kumar, B.; Mishra, V.; Singh, K. Hierarchically Structured CsPbBr$_3$ @Ti$_3$ C$_2$ T$_X$ Nanohybrid Frameworks for High-Performance Supercapacitors. *ACS Appl. Energy Mater.* **2026**, *9* (6), 3038–3052. https://doi.org/10.1021/acsaem.5c03596.

(24) Xu, S.; Wei, G.; Li, J.; Han, W.; Gogotsi, Y. Flexible MXene–Graphene Electrodes with High Volumetric Capacitance for Integrated Co-Cathode Energy Conversion/Storage Devices. *J. Mater. Chem. A* **2017**, *5* (33), 17442–17451. https://doi.org/10.1039/C7TA05721K.

(25) Rundla, A.; Priyanka; Kumar, B.; Tripathi, P.; Kumar, P.; Singh, K.

Ti3C2Tx MXene@rGO Composite Electrodes for High-Performance Supercapacitor Applications. *Journal of Power Sources* **2025**, *632*, 236408. https://doi.org/10.1016/j.jpowsour.2025.236408.

(26) Priyanka; Rundla, A.; Kumar, B.; Singh, M.; Rani, D.; Kumar, P.; Mishra, V.; Singh, K. Interfacial Engineering of $Ti_3 C_2 T_x$ -Protected $CsPbBr_3$ Perovskite Quantum Dots for Enhanced Charge Transport and Superior Hydrogen Evolution Catalysis. *Advanced Sustainable Systems* **2026**, *10* (4), e01283. https://doi.org/10.1002/adsu.202501283.

(27) Kumar, B.; Rundla, A.; Priyanka; Singh, M.; Rani, D.; Kumar, P.; Singh, K. Synergistic Ti3C2Tx MXene Quantum Dot/Nanosheet Hybrid: Elevating Supercapacitor Performance. *Journal of Power Sources* **2025**, *652*, 237603. https://doi.org/10.1016/j.jpowsour.2025.237603.

(28) De, S.; Acharya, S.; Maity, C. K.; Nayak, G. C. Boron Nitride/$Ti_3 C_2 T_x$ MXene Nanosheet/WS_2 Nanostructure Ternary Composites for All-Solid-State Flexible Asymmetric Supercapacitors. *ACS Appl. Nano Mater.* **2023**, *6* (13), 11175–11186. https://doi.org/10.1021/acsanm.3c01202.

(29) Singh, M.; Kumar, B.; Rundla, A.; Priyanka; Rani, D.; Kumar, P.; Singh, K. High-Performance 1T-WS2/rGO Composites with Enhanced Charge Storage Mechanism for Supercapacitor Applications. *Journal of Energy Storage* **2025**, *140*, 118945. https://doi.org/10.1016/j.est.2025.118945.

(30) Shen, L.; Zhou, X.; Zhang, X.; Zhang, Y.; Liu, Y.; Wang, W.; Si, W.; Dong, X. Carbon-Intercalated $Ti_3 C_2 T_x$ MXene for High-Performance Electrochemical Energy Storage. *J. Mater. Chem. A* **2018**, *6* (46), 23513–23520. https://doi.org/10.1039/C8TA09600G.

(31) Zhao, C.; Wang, Q.; Zhang, H.; Passerini, S.; Qian, X. Two-Dimensional Titanium Carbide/RGO Composite for High-Performance Supercapacitors. *ACS Appl. Mater. Interfaces* **2016**, *8* (24), 15661–15667. https://doi.org/10.1021/acsami.6b04767.

(32) Yoon, Y.; Lee, M.; Kim, S. K.; Bae, G.; Song, W.; Myung, S.; Lim, J.; Lee, S. S.; Zyung, T.; An, K. A Strategy for Synthesis of Carbon Nitride Induced Chemically Doped 2D MXene for High-Performance Supercapacitor Electrodes. *Advanced Energy Materials* **2018**, *8* (15), 1703173. https://doi.org/10.1002/aenm.201703173.

(33) Xu, S.; Wei, G.; Li, J.; Han, W.; Gogotsi, Y. Flexible MXene–Graphene Electrodes with High Volumetric Capacitance for Integrated Co-Cathode Energy Conversion/Storage Devices. *J. Mater. Chem. A* **2017**, *5* (33), 17442–17451. https://doi.org/10.1039/C7TA05721K.

Current Natural Sciences & Engineering
Volume 3, Issue 1, 2026, 964-976

Deep Learning for Marine Animal Recognition: A Comparative Study of CNN Architectures and Triplet Loss Optimization

Mir Ihrar Ali

Trine University, United States

Received date:22/09/2025, Acceptance date: 17/06/2026

***DOI:* http://doi.org/10.63015/3ai-2503.3.1**

Corresponding Author: ihrar2022@gmail.com

Abstract

The conservation of marine biodiversity has become. increasingly critical in the face of climate change and environ- mental degradation. Identifying individual animals is essential for understanding species behavior, migration patterns, and population dynamics, yet traditional methods remain time-intensive and reliant on expert observation. This study leverages deep learning to automate individual whale and dolphin identification using data from the Kaggle Happywhale challenge. The performance of several Convolutional Neural Network (CNN) architectures is evaluated, including ResNet, DenseNet, EfficientNet, and In- ceptionV3, and explore the combination of Softmax classification with a semi-hard triplet-loss approach. The results reveal that InceptionV3 achieves superior accuracy, while the hybrid Softmax and triplet-loss method offers limited benefits, hindered by dataset challenges such as the prevalence of hard triplets. These findings emphasize the need for refined loss strategies to handle unbalanced datasets in wildlife identification. This work highlights the potential of machine learning to revolutionize marine conservation efforts by enabling scalable and efficient individual recognition systems.

Keywords: Deep Learning, Kaggle Happywhale challenge, Marine biodiversity, Triplet-loss, Machine learning, Marine Conversation, Convoluational Neural Network Architectures (CNN)

1. Introduction

As climate change and environmental pollution intensify, nature conservation becomes increasingly important. A part of nature conservation is also the study of animal behavior, migration routes, and population density to better understand the problems and obstacles certain species are facing to tackle and prevent these problems to the best of the abilities. To do this, one must be able to differentiate between individuals of a species. In humans, this is easily done by face or fingerprint recognition. But what about animals? To date, researchers manually differentiate them by the shape and markings on their tails, dorsal fins, heads, and other body parts. This is time-consuming and difficult work since it takes the eye of a good researcher and much time to identify, match, or tell individual animals apart. Hence the question arises: When it is possible to use automated identification for humans, is there a similar approach possible for animals? The recent advances in facial recognition were mostly commercially motivated. Photo identification for animals seems like a less lucrative endeavour which moves it out of the research limelight. However, a technique like this could simplify the analysis of wildlife and therefore, nature conservation significantly. This is why it is decided to take on the Kaggle Happywhale challenge [1]. The goal of this challenge is to train a machine learning model to identify whales and dolphin's individuals. The competition model will be used on happywhale.com [2], a research collaboration platform that aims at increasing global understanding and caring for marine animals. This challenge is used to look for relevantly easy approaches that could be implemented by conservation organizations to automatically detect individuals on their datasets as well [3].

II. Kaggle happywhale challenge

In the following chapter, the Kaggle Happywhale challenge is explained. This includes goal setting and a comprehensive analysis of the dataset.

A. Goal

The Happywhale Challenge is a research prediction com- petition open to everybody with a Kaggle account. Its goal is to build a machine-learning model that can reliably recognize individual whales and dolphins. The model should also be able to classify individuals it has never seen before as” new.” Such a model would save experts, who - up until now - must analyze the images manually, a tremendous amount of work.

B. Data

The data [1] to be used for this challenge is split in to training and testing data. The training data consists of 51 thousand JPEG images of whales and dolphins. The training images are labelled with the according species and a unique individual identification string. The testing data consist of 28 unlabelled images containing some new whales and dolphins which are not present in the training data. Typical examples from the Happywhale dataset are shown in **Fig 1**.

In total there are about 15 thousand different individuals and 30 different species. This data was manually curated by researchers from all over the world.

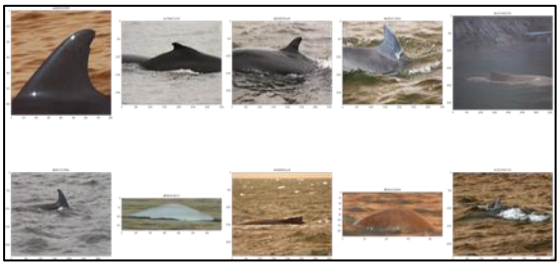

Figure 1: Typical images from the data set

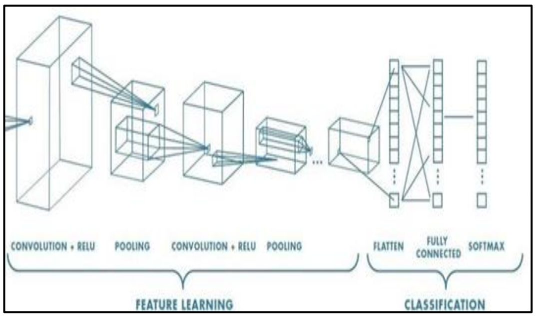

Figure 2: Vanilla image classification [7].

With a median image shape of approximately (3000,1500), most images have high resolution. This makes unique patterns and markings of each individual identifiable by a neural network, even though most images only contain small parts of the marine animals, such as dorsal fins and parts of the backs. Some further analysis shows that 59% of all individuals have only one image of themselves. They make out 18% of all images in the data set [4]. 5% of all individuals have at least 10 images of themselves. These are 47% of all images in the data set. This is a large unbalance in the number of images per individual and will make training the network much harder [5].

III. Model selection

At first glance, one could think that the problems like the Happywhale challenge are generic multi-class classification task. This would mean that the model should be able to classify an input image of an individual correctly as just this individual. For tasks like this, the default approach is the following: Feed the input image to some Convolutional Neural Network (CNN) architecture, which outputs an embedding of this image. This embedding can then be flattened and fed into a Dense Layer, which will output the predicted class. [6]. The conventional image-classification pipeline is illustrated in **Fig 2**.

A. CNN architecture

As a first step of model selection popular CNN architectures are compared to test. It is often a good idea to bet on architec- tures which already solidified their position on the grandstand of the machine learning domain of interest. Therefore, it is important to look at the most implemented models for image classification tasks. Looking at this list, a Residual Neural Network (ResNet) is decided, a Densely Connected Neural Network (DenseNet), an EfficientNet, and an InceptionNet. [8]. All these networks are notorious for being capable of classifying images with very high accuracy while being somewhat computationally efficient (at least compared to other machine-learning approaches).

Additionally, there are countless pre-trained models with easy access points available for these architectures. Especially the models pre-trained on ImageNet [9], one of the world's largest labelled image databases, are extremely powerful for image classification tasks and, therefore, of great interest to us.

It has been decided to try out the following architectures with pre- trained weights from ImageNet: ResNet50, ResNet50V2, DenseNet101, EfficientNet, and InceptionNetV3. We also trained ResNet50 us. More about that can be read in Softmax Model.

B. Softmax activation

The activation function of the last Dense Layer in this pipeline is usually a Softmax function [10], which computes a probability distribution σ over the image membership for each class K. The Softmax function is defined in Equation (1).

$$\sigma(Z_i) = \sum_{j=1}^{K} \frac{e_{zi}}{e_{zj}} \qquad (1)$$

for i = 1, . . . , K and $(z_1, \ldots, z_K) \in \mathrm{R}^K$

K is determined by the constant number of neurons in the final Dense Layer. Unfortunately, we are working with a dynamically changing number of classes - Every individual whale in the ocean (let alone have images of them) is not known. For now, this eliminates the Softmax activation function as a suitable approach to the task.

C. Triplet loss

Luckily, the domain of metric learning offers us an alternative approach that is more suitable for the problem: Triplet loss - originally presented in the FaceNet [11] paper.

The goal of triplet loss is to learn an embedding space in which similar sample pairs stay close together and dissimilar ones are far apart. It does this by computing a distance between an anchor image a and a positive sample p, as well as between a and a negative sample n. a and p are different images of the same individual, while n is an image of a different individual. A visualization of triplet loss is shown in **Fig 3**.

Figure 3: Triplet loss visualized [11].

The learning goal is then to minimize the distance between a and p and maximize the distance between a and n at the same time [12]. Triplet Loss for some triplet (a, p, n) in the embedding space is defined as: The triplet-loss objective is given in Equation (2).

$$L_{triplet} = \max(0, d(a, p) - d(a,n) + \epsilon) \qquad (2)$$

where d denotes the L2 norm (calculated from the Euclidean distance between the embeddings) and the margin parameter ϵ denotes the minimum offset between distances of d(a, n) and d(a, p). This prevents the network from gaming the function and circumventing its actual intention. If there was no ϵ, the network could just map the complete data set onto the same point in the embedding. This would cause all distances and the loss to be 0. The margin ensures that, in this case, the loss would still be positive. [13]

1) Triplet Mining: Of course, triplet loss is far from being a perfect method of choice as well. One of its main limitations is that during one comparison, only one negative example n is compared with the anchor a. The disregard of all other n could lead to an embedding space where some dissimilar pairs are still near each other - just because they were not compared against each other. [14] This is why, in order to train a triplet loss model successfully, one has to pay close attention to the composition of each triplet. To learn the model it should pick an n that is not obviously a different individual than a. To do this, a challenging n that is closer to the a than the positive sample p is chosen.

$$d(a, n) < d(a, p) \qquad (3)$$

This is called hard triplet mining. In theory, it should guarantee optimal learning success. However, it is prone to get stuck in local minima and the samples are rather hard to select from the data set. An approach that tries to solve this is semi-hard triplet mining. Here the triplets are chosen in a way, that n is not closer to a than p, but the function still has a positive loss. The hard-triplet condition is expressed in Equation (3).

$$d(a, p) < d(a, n) < d(a, p) + \epsilon \qquad (4)$$

The distance between a and n is still in the range of margin ϵ. This way, the model can still learn but is more unlikely to end up in local minima.

It is needed to specify the triplet sampling process even further by choosing between offline and online triplet mining. With offline mining, the triplets are generated at the beginning of each epoch. The embeddings are computed on the training set, and then only (semi-) hard triplets are selected. This technique is rather inefficient because it needs to do a full pass on the training set for each epoch and update the triplets. Doing online mining, samples are produced for each batch of inputs. Within a batch of B examples, this can find a maximum of B3 triplets. Many of these triplets are not of shape (a, p, n) and are therefore not valid. Still, it does not require updating all samples offline, and more samples are created for a single batch. This makes the approach way more efficient [15].

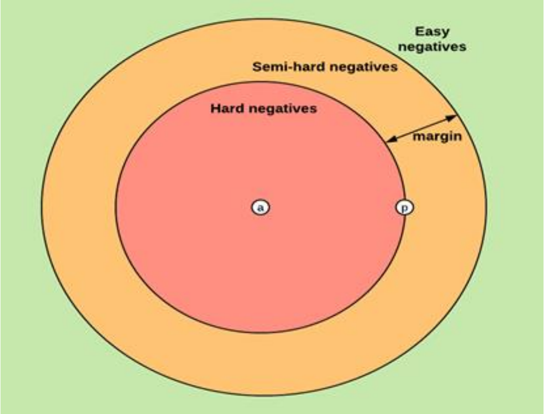

Figure 4: Different kind of Negatives visualised [15].

2) *Shortcomings:*

There remain problems with the triplet loss function and contrastive learning approaches in general. It is hard to guarantee that embeddings of the same individual will be pulled together in Euclidean space (expansion prob- lem). In addition, there is the so-called sampling issue [13]: Online triplet mining is hard to implement for very unbalanced data sets like the Happywhale data set. There are modern alternatives to triplet loss such as Cos- and ArcFace, which are based on angular distance and margin. They (partially) solve the above problems, but this nevertheless wanted to try out vanilla triplet loss. Since the paper should also be of some educational value and explain the concepts well to other students, triplet loss is also more suitable because it is less advanced and needs fewer prerequisites to understand. Because of the mentioned advantages in Triplet mining, this also decided to implement online semi-hard triplet mining. There is still one disadvantage of triplet loss which I did not talk about up until now: Evaluation of training progress is computationally expensive. As it is required to evaluate the useful- ness of the different CNN architectures, it needs to compute an evaluation metric (i.e. accuracy) on the validation set after each training epoch. To do this, the embedding of every image from the validation set needs to be compared to all embeddings of the training set. This means there have to be many point- wise distance calculations in a high dimensional Euclidean space calculated. To be specific, it needs to do $37598 * 4177$ computations in a 256-dimensional embedding space for each epoch. Furthermore, the convergence time for triplet loss models is said to be rather high. Doing this for more multiple hyperparameter settings for each architecture is not feasible with the computational resources. Is there a cheaper workaround? The semi-hard-triplet condition is expressed in Equation (4).

D. Combining Softmax and Triplet Loss

It is already found out that the Softmax activation function is not useful for the final model but maybe still utilize it for some architecture comparison. Computing the accuracy of a Softmax-based model is a breeze compared to models based on contrastive loss.

This can imagine that an architecture that performs well over a finite-class classification task using Softmax is also likely to perform well for a classification problem with a dynamical number of classes like Happywhale. So why not try this out? The approach used here will now look like the this:

I. *Research Questions*

Knowing all this, it can motivate the following hypotheses that it needs to investigate further:

1) Is a 'lazy' approach of just using prebuild & pre trained architectures and preconfigured loss functions sufficient to produce significant results in individual clas- sification?

2) Is Softmax classification training success a useful indica- tor for triplet loss training success? To be specific: Does the best performing CNN architecture under Softmax also show the best performance under triplet loss?

3) Can we reduce triplet loss training time with network weights pre-trained on Softmax classification?

II. Data pipeline

A. Preprocessing

This applies several preprocessing steps to get the data into an optimal shape for the model. There is also created One-hot labels.

1) Normalization: Normalization ensures that all images have the same format.

One of the first steps is downsizing the images. Although the mostly high-resolution pictures allow us to see patterns and unique marks of the whales in great detail, this has to downsize the images enough that the memory can handle it. It is also useful to have every image in the same quadratic shape. It has been selected the shape (224, 224) since it is small enough not to run into memory constraints but still large enough for the model to recognize some details. The pretrained ImageNet-models also use this input size. The automatic interpolation of Tensorflow ensures that the images still look somewhat natural and not too distorted.

The pixel values have been also converted from integers to floats to make sure that Tensorflow can work with them. The float values were fixed between -1 and 1.

2) Foreground Extraction: Since the images often contain much ocean in the background and the model should definitely not take this as feature, it would be a good idea to crop the background such that only the whale on white background is in the image. An example of failed foreground extraction is shown in **Fig 5**.

In this mainly used preexisting algorithm from the Kaggle Humpback Whale challenge [16] for this. Unfortunately, large parts of whales were cropped in many images.

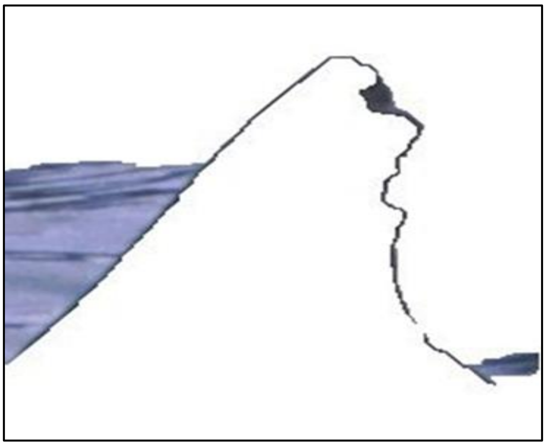

Figure 5: Failed foreground extraction

This is why We decided not to include this preprocessing step in the pipeline.

3) Data Augmentation: Data Augmentation has the goal of increasing the size of the data set.

This is especially useful for obtaining multiple images of whale individuals for which only one or two images exist. However, it was decided against data augmentation because it significantly impacted training speed - even though better results might be obtained with it.

It was decided to incorporate classic augmentation steps, such as random image flipping, contrast, and brightness, to introduce more randomness to the data. This might lead to a more regularized model performance. Being nit-picky, these steps also count under ”normalization,” but it needed to lay down the reasons for not doing data augmentation in a separate paragraph.

B. Dataset creation

Since online mining samples the triplets within one batch, to ensure on batch creation that there are sufficiently many different pairs of anchors and positives per individual within a batch. As analyzed earlier, there are many individuals with only one or two images in the Happywhale data set.

Suddenly, this turned out to be a quite interesting constraint satisfaction problem (CSP).

First, what to do with the individuals with only one image, which makes up 59% of all individuals and 18% of the dataset was considered. One approach could be to use image augmentation and then pair the individuals with an altered version of their images. However, since the model needed way too much time already, it has been decided to use these individuals not for training but for another process later.

1) Smart Batches Algorithm: To solve this CSP, it came up with an algorithm that can easily be generalized for other triplet loss applications.

First and foremost, it is decided to only accept an even batch size, which relaxes the CSP quite a lot.

It is chosen 64 as a batch size simply because it yielded the best performance - in terms of training time - on the setup (Nvidia GTX 1080).

Let’s consider N images of different animals, with at least two images per animal. It also has an even batch size b. It needs to divide by the number of batches, which is $\lceil N/b \rceil = M$. The last batch will not have size b but rather $M \% b = L$. Now, the N images over these batches to be distributed in such a way that there is never a single image of an individual in a batch and that one batch never contains images of only one individual.

The way this problem is solved by creating two separate pools. In the one pool, all the images of animals are put in with an even number of images, and in the other, all the animals with an uneven number of images. Then it was iterated through every animal in the uneven pool.

The first three images of every animal has been and keep them in the uneven pool. The even amount of rest can be thrown into the even pool.

For example, if a whale has 17 images, it will keep the first 3 pictures in the even pool and put the next $17 - 3 = 14$ pictures into the even pool.

Now, only triplets have left in the uneven pool.

For a healthy amount of randomness, it has been shuffled them around. For reproducibility, need to set a seed beforehand.

There is a small special case when N - and subsequently L-is uneven. The even pool still contains an even number of images. So, the only source for the unevenness of N can be in the uneven pool. This would mean that an uneven number of triplets. In this case just took the first triplet and putted it into the last batch.

This was enforced that:

1) Every batch has an even amount of space left.

2) There is an even number of images in the even pool

3) There is an even number of triplet-pairs in the (initially) uneven pool

This has been solved the CSP with this algorithm:

1) Combine the triplet pairs into pairs of 6 each.

2) Distribute them over the batches.

3) Form positive triplet-pairs of 2 in the even pool and shuffle them (with seed).

4) The batches with the triplet-pairs of 2 were filled up.

Because it has at least two or three images of every animal in a batch, as there is never a single image of an individual in a batch. Because it was shuffled the first pairs of two, one batch most likely never contains images of only one individual. If this is not the case, it can be simply chosen another seed. To now keep this order, it will make sure to not shuffle not to shuffle at a later step in the pipeline.

III. Softmax model

For training the Softmax model on species classification, it has been decided to use all available training images. For Softmax standards, 51000 images are not that many. This is why it is decided on a train/validation/test split of 0.8/0.1/0.1.

To train, validate, and evaluate or model predicting all 30 species, it is considered to have at least one image of every species present in every dataset. To achieve this, the Smart Batches Algorithm, is used simply because it is likely to create such a split. It named all functions with different seeds and quickly found the first valid candidate, ”5”, which It is then used for all Softmax models.

A. Configurations and Hyperparameters

All architectures loaded with the includetop setting as false and set pooling to max. It then simply put a dense layer with 30 neurons for the species and a Softmax activation function on top. This chose Adam as an optimizer with a learning rate of 0.001 and set Categorical Cross Entropy loss.

Nothing special - standard image classification settings.

B. Evaluation

1) ImageNet vs Random Weights: This first wanted to test whether loading the models with weights, which were pre-trained on the ImageNet dataset, would lead to faster convergence was trained. To do this, ResNet50 for 10 epochs each. Once with the pre-trained ImageNet weights and once with randomly initialized weights. The ImageNet weights beat the other in every metric. The comparison between ImageNet and random initialization is presented in **Fig 6**.

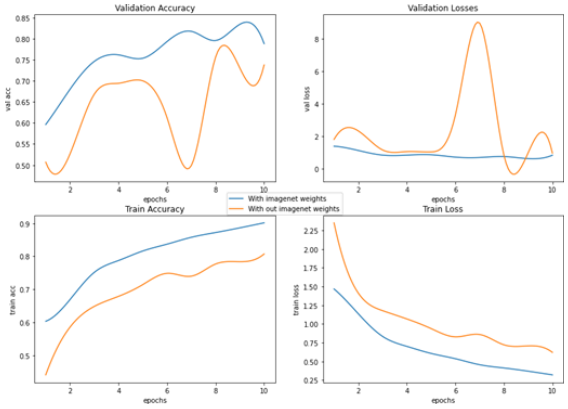

Figure 6: ImageNet vs random performance

Because of this, it has been decided stick to models with ImageNet weights for further analysis.

2) Comparing CNN architectures: Further, the performance is tested of several CNNs. As mentioned in CNN architecture, too many parameters not required so it could still train them locally. All architectures for 10-15 epochs were tested.

These were the results:

Table I: ACC10 denotes the validation accuracy after 10 training epochs. s =seconds.

Architectures	***ACC$_{10}$***	***s/epoch***	***ACC$_{10}$*/time**
ResNet50	81,9	532	0.15
ResNet50V2	85,4%	411	0.21
DenseNet100	89,7%	506	0.18
InceptionNetV3	90%	271	0.33

This has been also tried to use several versions of Efficient Net, but sadly, the kernel always died quickly.

As it can see, InceptionNetV3 had - compared to the others

An outstanding performance considering training time. This is why the model is selected, which further will trained and of which recycled the weights later for the Siamese Model Training.

It has been then decided to train for 70 epochs in total and evaluate the best model checkpoint with the best validation accuracy on the test dataset. This has been achieved a test accuracy of 94.45% and a k3-accuracy of 98.79% on the test data, which was quite impressive.

It is analyzed the accuracy for every species and found that, as one might expect, the model was good at recognizing species with many images while struggling with the uncommon ones.

For example, it completely failed to detect the least common species (" Frasier Dolphins" with only 14 images). Strangely, the best performing species were the" Commersons Dolphins", with only 90 images in the database. It assumes this has to do with the unique, black-and-white look of their dorsal fins and the very high image quality of the images, which you can see here.

IV. Triplet loss model

A. *Specific Dataset*

Since the Kaggle Challenge already provides a testing mechanism, a validation dataset was chosen. It was already disregarded more than half of individuals, so to throw away more data was not required. Hence, it was decided to only consider individuals with > 3 images. It was then used a method very similar to the Smart Batches Algorithm:

1) Iterate over all the individuals with > 3 images.

2) Take the first two images and put them to the side to make sure it don't disregard individuals.

3) Shuffle the remaining images (with a seed).

4) According to the split ratio S (We chose 0.1), take the first $\lceil S * \text{len(remaining images)} \rceil$ individuals as your validation dataset.

5) Use all the other images as the training dataset.

Then the Smart Batches Algorithm called and do the remaining standard preprocessing steps. The seed 0 is being used.

B. *Configurations and Hyperparameters*

To test the hypotheses, these models are trained:

a. InceptionV3 Model with the weights pre-trained on the Softmax species.

b. InceptionV3 with imagenet weights.

c. Resnet50V2 with imagenet weights.

d. For simplicity, it is referred to the models from now on as" Species-Weights"," ImageNet-Weights" and" Control- Model".

e. As for the embedding block, which is put on top of the CNN, it is chosen this architecture: 3 Dense-Layers with 512, 256, and 256 output neurons, respectively, and ReLu - activation functions. Then choosen to use an l2-normalizing layer as the final output layer to enforce more evenly distributed distances to then later be able to better identify new individuals.

f. An automated online semi hard triplet mining with a default margin of 1 was done.

C. *Evaluation*

1. Procedure: Since the Kaggle Challenge offers a nice automatic way of testing models, this had to only come up with a validation procedure for the inter-model comparison. It was decided on this 2-stage validation procedure:

Firstly, since the model should learn to recognize individuals, it has seen before, It was decided to measure the accuracy of the images of the known individuals being correctly matched, as well as the k5-individual accuracy and the accuracy of classifying the right species. To achieve it has been calculated the embeddings of the train and validation datasets. Then, computed the pairwise distance matrix with a Euclidean metric of the two embeddings and sorted out the labels with the 5 closest values. With these labels, now calculated the previously mentioned accuracies. In addition, used UMAP to visualize a dimensional representation of the embeddings. Secondly, the model should also recognize when it has not seen an individual before. For that, used the individuals with only one picture and calculated their embeddings. Then calculated the pairwise distance matrix of those embeddings with the train embeddings and sorted out the distance to the nearest neighbour. Then compared this distance to the average distance of individuals, which the model is already familiar with. For that, created density plots of the distributions.

2. Analyzing General Training Behaviour: When looking at these results in Figure 7 this were initially surprised. Why does every model shows its best performance before training? Therefore some data analysis done:

Before training, all the weights of the embedding block are randomly initiated. Thus, a high Validation Accuracies arises probably from the very uneven distribution of individual counts. First, to look at the dataset used for the Siamese model training and validation, the dataset containing all the individuals with at least 2 images. The top 300 individuals of this data make out 5% of the individuals and 40% of the images. So, if chose random images from the data, the chances of getting the same individual are quite high. Even more interesting is to which species these most 300 common individuals belong to:

This can be clearly seen, that these top 300 individuals belong mainly to the most frequent classes. The validation accuracies obtained during training are shown in **Fig 7**.

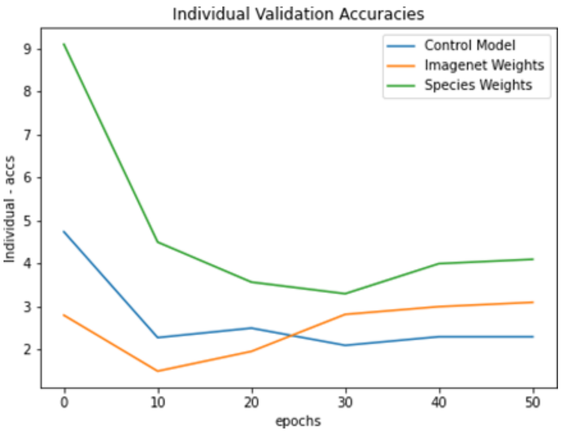

Figure 7: Individual Validation Accuracies

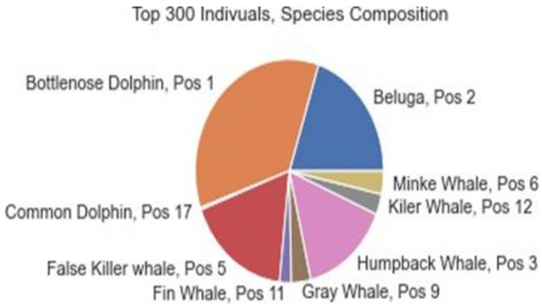

Figure 8: Species Composition of top 300 Individuals. Pos refers to the degree of frequency to the most frequent classes.

In addition, what is very interesting is that the species accuracy, the likelihood of the next neighbor in the embedding space being of the same space, is for all models around around 80% after epoch 30. If combined these two facts, it can refer that the most frequent classes are quite densely packed together in the embedding space. Therefore, the images of the 300 most common individuals, which make out a huge part of the training data, are also most likely in those densely packed embedding spheres. It is assumed that, therefore, a lot of ”Hard-Triplet-Pairs” within these spheres of the most frequent species. And since training on ”Semi-Hard-Triplets,” the theory now is that the initial accuracy of the model decreases because it arises from correctly matching the most frequent individuals, which the model is then not trained to do. In addition, the 2d UMAP plots of the embeddings support this hypothesis.

1) Species Weights vs ImageNet Weights: All three validation accuracies (Individual, k5-Individual, Species) and also the 2d-UMAP-plots before and while training shows that the Species Weights Model performs significantly compared to the Imagenet-Model.

2) Species Weights vs ImageNet Weights: All three validation accuracies (Individual, k5-Individual, Species) and also the 2d-UMAP-plots before and while training shows that the Species Weights Model performs significantly compared to the Imagenet-Model.

3) Imagenet Weights vs Control Model: Although the InceptionV3 Model outperforms the Resnet50V2 model in terms Individual and k5 accuracy the effect is by far not as strong in the Softmax case. Especially if I take into account that it took the InceptionV3 model almost double as long as the Control Model to have a convergent training loss.

D. Kaggle Test Dataset Evaluation

Since the best performing model is, quite ironically, the Species-Model before training even one epoch with the triplet loss, chosen it for the test evaluation. To now test the model, it had to create a submission.csv according to this guideline. Most importantly is that it is not only have to identify individuals which has seen before, but also new individuals. For that, used the density plot of the average distance of new individuals to their next neighbors compared to known individuals. Looking at the distributions decided to expect there to be a new individual at a distance of 0.35. To generate the submission.csv now first had to compute the embeddings of all the data (the Kaggle training data) and the embeddings of the Kaggle test data. Then, computed the pairwise distance matrix and sorted out the 5 closest neighbors and their corresponding labels. For every test image I know, iterated through the list of the 5 closest neighbors. If the distance to the neighbor was bigger than 0.35, inserted ”newindividual” into the list at that position. Like this We achieved a score of 0.077.

V. Conclusion

A. Hypothesis 1

Is a ”lazy” approach of just using prebuild & pre-trained architectures and preconfigured loss functions sufficient enough to produce significant results in individual classification?

With a final Kaggle Evaluation Score of 0.077, the model did really not achieve sufficient result to be use full in anyway in marine nature conservation. Therefore, it is assumed that a similar approach is most likely also not sufficient enough for other domains of nature conservation.

B. Hypothesis 2

Is Softmax classification training success a useful indicator for triplet loss training success? To be specific: Does the best performing CNN architecture under Softmax also show the best performance under triplet loss?

With the InceptionV3 model with imagenet weights just barely outperforming the Resnet50V2 model with imagenet weights in regard to validation accuracy, it does not have enough data to either support or deny this hypothesis.

C. Hypothesis 3

Can you reduce triplet loss training time with network weights pre-trained on Softmax classification?

Because of the strong performance of the InceptionV3 Model pre trained on classifying the whale and dolphin species compared to the other models, and have strong reason to follow this hypothesis.

Acknowledgment
The author would like to thank the Kaggle Happywhale challenge community for providing the dataset and resources used in this study.

Conflict of Interest
The author declares that there is no conflict of interest regarding the publication of this paper.

References

[1] Kaggle, "Happywhale - whale and dolphin identification," 2022, visited on 2022-04-01. https://www.kaggle.com/c/ happy-whale-and-dolphin

[2] n.d., 2022, visited on 2022-04-01. https:// happywhale.com

[3] S. Malhotra, "Self-organizing interaction spaces: A framework for engineering pervasive applications in mobile and distributed environments," 2025. https://arxiv.org/abs/2502. 01137

[4] A. Awasthi, "Leveraging gans for active appearance models optimized model fitting," 2025. https://arxiv.org/abs/2501. 11218

[5] M. Cherukuri, "Comparing image segmentation algorithms," in 2024 IEEE 4th International Conference on Data Science and Computer Application (ICDSCA), 2024, pp. 266–269.

[6] L. Schmid, R. Horn, C. Lange, M. Pink, and K. Kobrock, "05 introduction to cnns,"http://www.studip.uni-osnabrueck.de, University of Osnabrueck, 2021, visited on 2022-04-01.

[7] P. Raghav, "Neural network with many convolutional layers," 2018, visited on 2022-04-01. https://miro.medium.com/ max/1200/1*XbuW8WuRrAY5pC4t-9DZAQ.jpeg

[8] Meta Platforms, "Image classification," 2022, visited on 2022-04-01. https://paperswithcode.com/task/ image-classification#papers-list

[9] J. Deng, W. Dong, R. Socher, L.-J. Li, K. Li, and L. Fei-Fei, "Imagenet: A large-scale hierarchical image database," in 2009 IEEE conference on computer vision and pattern recognition. IEEE, 2009, pp. 248–255.

[10] L. Schmid, R. Horn, C. Lange, M. Pink, and K. Kobrock, "02 training nns," http://www.studip.uni-osnabrueck.de, University of Osnabrueck, 2021, visited on 2022-04-01.

[11] F. Schroff, D. Kalenichenko, and J. Philbin, "FaceNet: A unified embedding for face recognition and clustering," in 2015 IEEE Conference on Computer Vision and Pattern Recognition (CVPR). IEEE, jun 2015, visited on 2022-04-01.https:

//doi.org/10.1109%2Fcvpr.2015.7298682

[12] L. Weng, "Contrastive representation learning," lilianweng.github.io, 2021, visited on 2022-04-01. https://lilianweng. github.io/posts/2021-05-31-contrastive#triplet-loss

[13] C. Kha Vu. (2021) Deep metric learning: A (long) survey. Visited on 2022-04-01. https://hav4ik.github.io/articles/ deep-metric-learning-survey

[14] K. Sohn, "Improved deep metric learning with multi-class n-pair loss

objective," in Advances in Neural Information Processing Systems,

D. Lee, M. Sugiyama, U. Luxburg, I. Guyon, and R. Garnett, Eds., vol. 29. Curran Associates, Inc., 2016, visited on 2022-04-01. https://proceedings.neurips.cc/paper/2016/file/ 6b180037abbebea991d8b1232f8a8ca9-Paper.pdf

[15] O. Moindrot. (2018) Triplet loss and online triplet mining in tensorflow. Visited on 2022-04-01. https://omoindrot.github.io/ triplet-loss#triplet-mining

[16] A. D. Kapse, "Foreground extraction-opencv," 2020, visited on 2022-04-01. https://www.kaggle.com/code/akhileshdkapse/ foreground-extraction-opencv/notebook

CNS&E

Current Natural Sciences & Engineering